Origins of twin boundaries in additive manufactured stainless steels

Y. Nie, Y.T. Chang, M.A. Charpagne

PII: S1359-6454(24)00387-2

DOI: https://doi.org/10.1016/j.actamat.2024.120035

Reference: AM 120035

To appear in: Acta Materialia

Received date: 24 February 2024 Revised date: 17 May 2024 Accepted date: 22 May 2024



Please cite this article as: Y. Nie, Y.T. Chang and M.A. Charpagne, Origins of twin boundaries in additive manufactured stainless steels, *Acta Materialia* (2024), doi: https://doi.org/10.1016/j.actamat.2024.120035.

This is a PDF file of an article that has undergone enhancements after acceptance, such as the addition of a cover page and metadata, and formatting for readability, but it is not yet the definitive version of record. This version will undergo additional copyediting, typesetting and review before it is published in its final form, but we are providing this version to give early visibility of the article. Please note that, during the production process, errors may be discovered which could affect the content, and all legal disclaimers that apply to the journal pertain.

© 2024 Published by Elsevier Ltd on behalf of Acta Materialia Inc.

### Origins of twin boundaries in additive manufactured stainless steels

Y. Nie<sup>a</sup>, Y.T. Chang<sup>a</sup>, M.A. Charpagne<sup>a,\*</sup>

<sup>a</sup>Department of Materials Science and Engineering, University of Illinois at Urbana-Champaign, USA

#### Abstract

316L and 304L stainless steels and a compositional gradient of both are fabricated using the same processing parameters via laser directed energy deposition additive manufacturing. In those alloys, the increase in chromium-to-nickel ratio is accompanied with grain refinement and formation of a high density of twin boundaries, i.e.  $\Sigma$ 3 boundaries. By means of electron microscopy, crystallographic and thermodynamic calculations, we demonstrate that two mechanisms arising from the ferrite-to-austenite solidification mode are at the origin of twin boundary formation and grain refinement: 1) inter-variant boundaries emerging from the encounter of pairs of austenite grains formed from a common ferrite orientation with Kurdjumov-Sachs orientation relationship; 2) icosahedral short-range-ordering-induced (ISRO) nucleation of twin-related  $\gamma$  grains directly from the solidifying liquid. These findings define new routes to achieve grain boundary engineering in a single step in FeCrNi alloys, by tailoring the solidification pathway during the AM process, enabling the design of functionally graded materials with site-specific properties.

Keywords:, stainless steel, additive manufacturing, twin boundaries, phase transformations, local liquid ordering

#### 1. Introduction

Grain boundary engineering (GBE) is a thermo-mechanical processing strategy that aims to introduce a high fraction of low energy boundaries [1]. These are commonly associated with coincident site lattice (CSL) boundaries and denoted with  $\Sigma$  followed by a number, in accordance with the reciprocal number density of lattice sites shared by both crystals [2]. In face-centered cubic (FCC) metals and alloys, twin boundaries are defined as a 60° rotation around a  $\langle 111 \rangle$  crystallographic direction and separate crystals that have one-third of their lattice sites in common. They thus belong to the  $\Sigma$ 3 family [3]. These low-energy boundaries disrupt the network of random grain boundaries, mitigating grain boundary-related deterioration such as crack propagation, intergranular corrosion, or hydrogen embrittlement [2, 4–9]. Most GBE methods rely on multiple deformation and annealing cycles, which is time and energy-consuming [10]. Furthermore, GBE is limited to relatively small specimen sizes with simple geometry [5, 11]. These many shortcomings have impeded the scalability of GBE so far [5].

Enabling near-net shaping in a single step, laser additive manufacturing (AM) represents a paradigm shift in metal processing. Extensive efforts have been aimed at mitigating printing defects, which has led to a dramatic reduction in

Preprint submitted to Acta Materialia

<sup>\*</sup>corresponding author

Email address: mcharp@illinois.edu (M.A. Charpagne)

defect size and density. Consequently, the mechanical properties of AM metals are now prominently governed by their microstructure [12–14]. Understanding the evolution of the microstructure and being able to tailor it in AM poses an outstanding challenge due to the complex thermomechanical history experienced by the material [15, 16]. The highly localized melting accompanied by rapid heating and cooling cycles induce large spatial variations in temperature gradient and unavoidably causes thermal strain [17]. Zou et al. recently demonstrated that during directed energy deposition (DED) of 316L, the accumulated thermal strain and temperature can reach up to 7% and 0.5 ( $T/T_m$ ), respectively [17]. Such conditions may induce dynamic recovery and promote both discontinuous and continuous dynamic recrystallization (DDRX, CDRX) in the previously deposited layers. These recrystallization mechanisms are characterized by the bulging of pre-existing grains and sub-grain rotation [17]. Evidence of CDRX and DDRX has been reported in other DED alloys [18]. Nevertheless, low CSL boundaries were not reported and are not apparent in these as-fabricated FCC alloys [17, 18].

Several solutions have been proposed to introduce twin boundaries in AM microstructures, primarily by triggering static recrystallization. Post-build annealing is relatively common, either as a single recrystallization treatment [19] or with added pressure via hot isostatic pressure (HIP), which also alleviates some defects. Yet, achieving full recrystallization in laser AM microstructures typically requires annealing at high homologous temperature for extensive amounts of time, sometimes at over 95% of the alloy's melting point [20, 21]. These are direct consequences of the high activation energy of static recrystallization in AM materials as well as sluggish grain boundary migration [22]. The slow recrystallization kinetics and relatively coarse grain structure typically obtained after annealing are key signatures of a sparse distribution of nucleation sites throughout the as-built microstructure, as well as a low driving force for strain-induced grain boundary migration [23]. This can be attributed to the occurrence of dynamic recovery during printing [24], a competing phenomenon to recrystallization that consumes its driving force, the stored strain energy, without any grain nucleation nor growth. Furthermore, dislocations typically arrange themselves in cellular structures in AM microstructures, that overlap with the microsegregation pattern arising from rapid solidification. These cellular structures are remarkably thermally stable [15] and unlikely to form sub-grains, the precursors of recrystallization nuclei, during annealing. In summary, the sluggish kinetics associated with static recrystallization render the incorporation of twin boundaries in additively manufactured materials through annealing treatment both time and energy-consuming.

As in conventional GBE processing, the dislocation density can be increased by adding an extra rolling step as part of the printing process, prior to annealing [25, 26]. Gao et al. [5] have studied in details the amount of mechanical strain that needs to be added for full recrystallization in 316L stainless steel manufactured by laser powder bed fusion (LPBF). They found that minimal amounts of strain are actually required to reach full recrystallization during post-build annealing, of the order of a few percent. They found that the exact amount of mechanical deformation directly scales with the size of the dislocation cells, hence depends on the scanning strategy: the coarser the cell structure, the lower the degree of solute segregation, thus resulting in a weaker barrier to the growth of recrystallized grains [5].

Strain levels below these critical amounts lead to abnormal grain growth via critical recrystallization [27]. To lower the

energy barrier to recrystallization directly during the AM process, Gao et al. [28] recently proposed a new scanning strategy to disrupt the cellular solidification patterns, hence their thermal stability, in LPBF 316L. Using this technique, they are able to reach full recrystallization upon subsequent annealing within reasonable times and temperatures. When integrated into an overall printing sequence, this strategy allows for "programmable" microstructures with site-specific recrystallization in three dimensions, without any mechanical deformation involved.

Here, we propose a new strategy for incorporating twin boundaries in as-solidified microstructures of FeNiCr alloys, in-situ during AM, and in a single step. It relies on manipulating the chemical composition of the material to tune its solidification pathway and form transient  $\delta$  ferrite upon cooling. This method allows for the formation of a dense network of twin boundaries in the as-built microstructure. We demonstrate this approach in a gradient made of 316L and 304L alloyed on-the-fly via laser DED. Using multi-scale electron microscopy, crystallographic considerations and thermodynamic calculations we elucidate the metallurgical mechanism that governs microstructure development. This finding opens new opportunities in alloy design for AM, and defines new pathways for GBE in a single manufacturing step.

#### 2. Materials and Methods

Nitrogen-atomized 304L and 316L powders with a particle diameter between 45 µm - 105 µm were purchased from Carpenter Technologies. Their respective compositions, as certified by the manufacturer, are expressed in weight  $percent\ as\ follows.\ 304L:\ Fe-18.62\%Cr-9.52\%Ni-1.3\%Mn-0.02\%Cu-0.75\%Si-0.018\%C-0.02\%O-0.01\%P-0.004\%S-0.02\%O-0.01\%P-0.004\%S-0.02\%O-0.01\%P-0.004\%S-0.02\%O-0.01\%P-0.004\%S-0.02\%O-0.01\%P-0.004\%S-0.02\%O-0.01\%P-0.004\%S-0.02\%O-0.01\%P-0.004\%S-0.02\%O-0.01\%P-0.004\%S-0.02\%O-0.01\%P-0.004\%S-0.004$ 0.07%N; 316L: Fe-17.6%Cr-12.6%Ni-0.89%Mn-2.43%Mo-0.67%Si-0.019%C-0.02%O-0.007%P-0.004%S-0.09%N. Block-shaped 304L, 316L, and functionally graded specimens with a geometry of 1.2 cm (width) x 2.5 cm (length) x 3 cm (height), were built on a low carbon steel plate using a Formalloy L2 DED system equipped with two feeders and a 1kW Nd: YAG laser with a wavelength of 1070 nm and Gaussian energy profile. The functionally graded material (FGM) is composed of 5 contiguous regions, each containing 24 deposited layers, and having a composition of  $304L_x316L_{1-x}$ . The gradient was deposited from bottom to top, with a 304L volume fraction x varying from 0.1 to 0.9 in 0.2 increments. A laser power of 500 W, scanning speed of 1100 mm/s, and step height of 0.25 mm were used to print all specimens, with a 90 ° scan rotation between layers. Argon was used as both the carrier and shielding gas. The specimens were removed from the build plate using a band saw, mechanically polished using abrasive papers, and then polished with diamond, alumina, and colloidal silica suspensions with a diameter down to  $0.05 \mu m$ .

A Thermo Fischer Scientific (TFS) Scios 2 scanning electron microscope (SEM) equipped with an Edax Hikari Super electron back-scatter diffraction (EBSD) camera featuring a charged-coupled device (CCD) detector of 640 x 480 pixels was used to characterize all microstructures. Each EBSD dataset was collected using an acceleration voltage of 20 kV and maps out at least 850 grains for statistical significance. The EDAX OIM Analysis software was used for EBSD data processing. Depending on their misorientation angle, grain boundaries are classified as low angle grain boundaries (LAGBs) or high-angle grain boundaries (HAGBs). The former are defined by misorientation

angles between 2-10°, while the latter possess a misorientation angle greater than 10°.  $\Sigma 3$  boundaries are defined using Brandon's criterion, with an angular tolerance of 8.66° from the ideal twin relationship [3, 29]. The  $\Sigma 3$  length fraction, defined using Equation(1), is used to quantify the density of  $\Sigma 3$  boundaries in the microstructure. Backscatter electrons (BSE) images were collected using a TFS Helios NanoLab 600 SEM/FIB DualBeam system under an acceleration voltage of 5 kV. Electron transparent specimens were prepared using twin-jet polishing in an  $HClO_4$  acid mix chilled to -30°C. Electron transparent samples were characterized using TFS Talos F200X transmission electron microscope (TEM) operated at 200 kV and equipped with a 4k x 4k  $Ceta^{TM}$  16M camera. Thermodynamic calculations were performed using the ThermoCalc 2023b software with the TCFE Steels/Fe-Alloys v13.1 database.

$$\Sigma 3 \text{ length fraction} = \frac{\text{total length of } \Sigma 3 \text{ boundaries}}{\text{total HAGB length}}$$
 (1)

#### 3. Results

#### 3.1. Microstructure statistics

The microstructures of as-printed 316L and 304L are shown in figure 1a,b using inverse pole figure (IPF) maps from EBSD. The build direction (BD) is normal to the observation plane. Both materials exhibit a relatively random texture along the build direction.  $\Sigma$ 3 boundaries are highlighted with black lines in both maps. 316L visibly exhibits an extremely low  $\Sigma$ 3 boundary density, consistent with previous observations [30], while 304L shows a much higher  $\Sigma$ 3 density. The cumulative grain size distributions of both alloys are plotted in figure 1c. Despite a similar distribution profile, a drastic reduction in grain size is observed in 304L, despite being fabricated using identical processing conditions. The most striking difference between the two alloys lies in their grain boundary misorientation distribution, shown in figure 1d and superimposed with the Mackenzie distribution of a random cubic polycrystal [31].

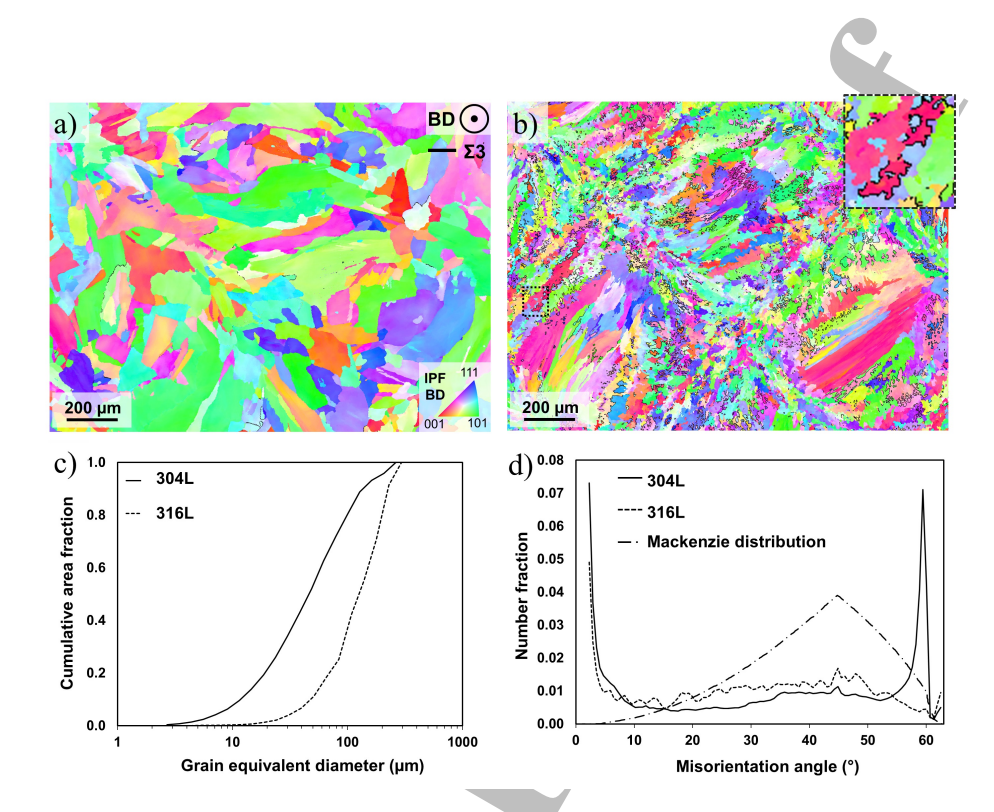


Figure 1: a,b) EBSD IPF maps showing the microstructure of as-printed a) 316L and b) 304L, c) grain size distribution of both materials, d) grain boundary misorientation distributions, along with the Mackenzie distribution of a random FCC polycrystal.

None of the alloys possess a random misorientation distribution. Instead, they both display a high fraction of LAGBs, which arises from the coalescence of solidification cells or dendrites that accumulate misorientation during crystal growth [5, 13, 32]. The main difference between the misorientation distributions of the two alloys is the presence of a strong peak around  $60^{\circ}$  in 304L, with a density of 0.071. This corresponds to the  $\Sigma$ 3 boundaries highlighted in black in figure 1b. With a density of 0.004, the 316L sample presents virtually no  $\Sigma$ 3 boundaries. To the best of our knowledge, the presence of  $\Sigma$ 3 boundaries in 304L fabricated by any AM technique has not been reported so far. Amid the complex thermal and mechanical history of these AM microstructures, we investigate the possibility of the occurrence of three classical twinning mechanisms in the following sections: annealing twinning, deformation twinning, and phase transformation-induced twinning.

#### 3.2. Annealing or deformation twinning

FCC materials with low to medium stacking fault energy (SFE) ( $\leq 45mJ/m^2$ ) such as 304L and 316L, are prone to forming  $\Sigma$ 3 boundaries during thermo-mechanical processing, i.e. sequences of rolling or forging, followed by thermal annealing [33–37]. Also called annealing twin boundaries, they typically form via strain-induced boundary

migration (SIBM) [38]. Amongst all formation mechanisms proposed, Pande's growth accident theory is the most commonly adopted [39]. This model asserts that a coherent twin boundary forms at a migrating grain boundary from a stacking error. AM-fabricated materials experience a complex thermal and mechanical history that arises from highly localized melting and solidification under high cooling rates (10³ - 10⁵°C/s typically [15]), followed by cyclic reheating from the deposition of adjacent tracks and subsequent layers [4, 40, 41]. These rapid heating and cooling cycles result in thermal stresses, manifest themselves via accumulation of intragranular orientation gradients and a high density of dislocations [4, 15, 41, 42]. In other words, the AM process inherently induces thermal-mechanical cycling. Previous research has provided evidence of SIBM and dynamic recrystallization during DED AM, in FCC materials with low to medium stacking fault energy. However, annealing twins are not reported and are not apparent in these as-built microstructures [17, 18]. From a crystallographic standpoint, annealing twins usually adopt a planar morphology [2, 3, 38]. This differs from the wavy morphology and globular twin domains observed in the insert of figure 1b. This peculiar morphology also rules out deformation twins, that typically adopt a needle-like or lenticular morphology as they grow [43]. Thus, the observed twin boundaries in AM 304L are neither annealing nor deformation twins.

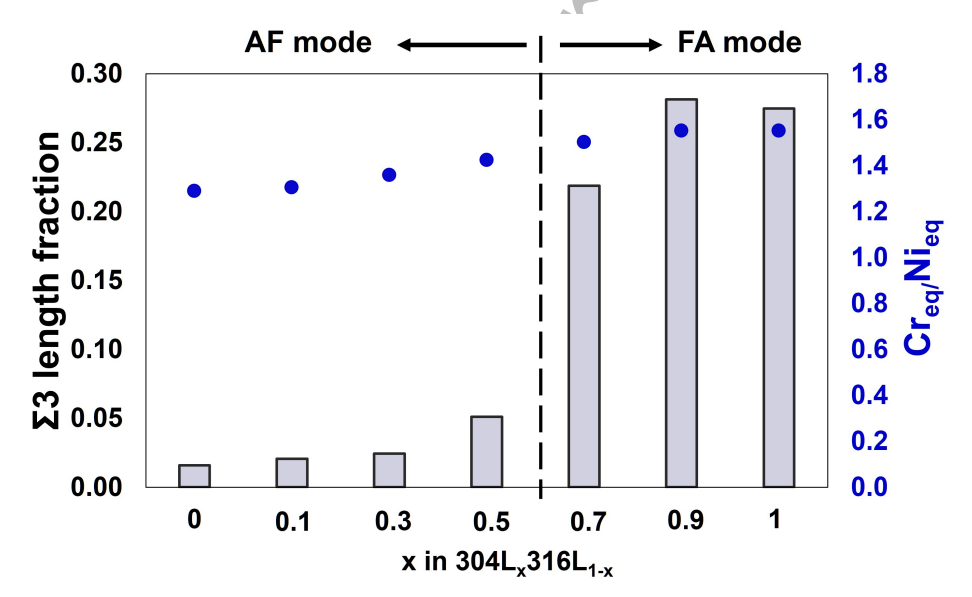


Figure 2:  $\Sigma 3$  length fraction and  $Cr_{eq}/Ni_{Eq}$  ratio as a function of 304L content in the functionally graded specimen. The dashed line indicates the transition between AF and FA solidification modes.

3.3. Phase transformation-induced twin boundary formation

To explore the origin of the drastic microstructure change from 316L to 304L, we printed a 316L-304L gradient with 20% increments of 304L in volume ratio, by mixing powders on-the-fly during printing. The  $\Sigma$ 3 boundary length fraction, defined by Equation (1), is measured via EBSD and plotted for different regions of the gradient, and shown in figure 2. Each bar in figure 2 contains over 100 mm of HAGB length. A slight increase in  $\Sigma$ 3 boundary fraction from 0.016 to 0.051 is observed as the 304L fraction increased from 0 to 0.5. Interestingly, when increasing the 304L fraction from 0.5 to 0.7, the  $\Sigma$ 3 boundary increases about 4-fold, reaching 0.219, despite only a slight change in composition. This fraction keeps increasing with further addition of 304L, reaching a value of 0.28.

The as-build microstructure of stainless steels is largely affected by the solidification mode [44], which is governed by the ratio between ferrite and austenite stabilizers,  $Cr_{eq}/Ni_{eq}$ . These are defined as  $Cr_{eq} = Cr + Mo + 1.5Si + 0.5Nb$  and  $Ni_{eq} = Ni + 30C + 30N + 0.5Mn$  in the Delong-revised Shaffler diagram, where each element fraction is expressed in weight % [45–47]. With increasing  $Cr_{eq}/Ni_{eq}$  ratio, stainless steel solidifies in four different modes: purely austenitic (A), austenite-to-ferrite (AF), ferrite-to-austenite (FA), and purely ferritic (F) [48]. We have previously demonstrated that DED-printed  $304L_x316L_{1-x}$  mixtures alloyed on-the-fly solidify at the transition between AF and FA [44]. Alloys with a volume fraction of  $304L \times 10^{-2}$  up to 0.5, solidify following an AF mode, while 304L-rich alloys with x > 0.5, solidify following a FA mode under the printing conditions employed here. The transition between the two solidification modes, highlighted with a dashed line in figure 2, shows a clear correlation with the steep increase in  $\Sigma 3$  boundary fraction.

In the FA solidification mode, body-centered cubic (BCC)  $\delta$  ferrite is the primary phase that solidifies. Upon cooling,  $\delta$  ferrite transforms to  $\gamma$  via a solid-state phase transformation [48]. Under the rapid cooling rates encountered in AM or welding, the  $\delta \to \gamma$  phase transformation is oftentimes incomplete and leads to remnant  $\delta$  ferrite trapped in the final microstructure [44, 49, 50]. A representative example of a FA-type microstructure is presented in figure 3a in 304L, where  $\delta$  ferrite particles are found on solidification cells and grain boundaries [44, 51, 52]. The  $\delta \to \gamma$  solid-state phase transformation generally takes place following preferred crystallographic orientation relationships (OR) that minimize the interfacial energy between the two phases [53, 54]. Common ORs include the Kurdjumov-Sachs (K-S) relationship, where  $\{111\}_{\gamma}//\{110\}_{\delta}$  and  $\langle 110\rangle_{\gamma}//\langle 111\rangle_{\delta}$ , and the Nishiyama–Wassermann (N-W) relationship, where  $\{111\}_{\gamma}//\{011\}_{\delta}$  and  $\langle 101\rangle_{\gamma}//\langle 100\rangle_{\delta}$ , or equally  $\{111\}_{\gamma}//\{110\}_{\delta}$  and  $\langle 112\rangle_{\gamma}//\langle 110\rangle_{\delta}$  [55–58]. For a given  $\delta$  orientation, 24 K-S and 12 N-W crystallographically equivalent  $\gamma$  grains -or variants "V"- can form.

In the following, we explore whether the encounter of two  $\gamma$  variants transformed from a single  $\delta$  ferrite orientation could lead to the formation of  $\Sigma 3$  boundaries. Tables 1 and 2 list the full enumeration of K-S and N-W variants, respectively. In each table, we name the first variant V1 (e.g. the  $(111)_{FCC}/(011)_{BCC}$  and  $[\bar{1}01]_{FCC}$ ,  $[\bar{1}\bar{1}1]_{BCC}$  for K-S) and use it as a reference to calculate intervariant axis/angle desorientation. The fourth column in both tables corresponds to the axis/angle desorientation between two  $\gamma$  variants inherited from a single  $\delta$  parent orientation, as they grow and impinge one another. Amongst the list of axis/angle pairs, the K-S V1/V2 pair corresponds to a 60° rotation around a  $\langle 111 \rangle$  direction, therefore a  $\Sigma 3$  boundary. This is the only twin configuration within the list of

all K-S and N-W variants. The right two columns in these tables show the inter-variant boundary length measured directly from EBSD data in our 316L and 304L printed samples, using a maximum angular tolerance of  $2^{\circ}$  from the ideal axis/angle relationship [56]. In 316L, all K-S and N-W variants are equally represented and their fraction is below 0.67%, which corresponds to a uniform distribution, in accordance with figure 1d. These low numbers suggest a complete absence of K-S or N-W OR in 316L, consistent with an AF solidification mode in this alloy. In 304L, the V1/V2 K-S rational boundaries represent 14.84% of the total boundary length and are by far the strongest variant detected. The length fractions of all other variants are close to the values detected in 316L, hence not statistically significant. This suggests either a near total V1/V2 variant selection during the  $\delta \rightarrow \gamma$  transformation, if solid-state phase transformation is the sole cause of  $\Sigma$ 3 boundary formation. A relatively strong V1/V2 selection has been previously reported by Haghdadi et al. [56], during cooling following thermal annealing in wrought 2205 duplex stainless steel. The K-S V1/V2 appeared as the prominent variant, and formed 10 to 100 times more frequently than any other variants. Here, tables 1 and 2 indicate a nearly 300-fold prevalence in K-S V1/V2 selection in AM 304L when comparing its boundary percentage (14.84%, in the right column) with that of any other K-S or N-W rational boundaries (typically less than 0.4%).

As a few volume percent of  $\delta$  ferrite remains in the 304L microstructure, shown in figure 3a, we investigate its OR with the surrounding  $\gamma$  grains. Figure 3 presents all ORs found in our 304L samples. A first type of OR is shown in the bright field TEM image in figure 3b, where a  $\delta$  particle is sitting on the grain boundary between two  $\gamma$  grains. A selected area electron diffraction (SAED) pattern was collected around the circled area, shown in figure 3c. The pattern reveals clear alignment of the [11 $\bar{2}$ ]  $\gamma$  axis with the [011]  $\delta$  axis. The (111)-type  $\gamma$  and (011)-type  $\delta$  diffraction spots are superimposed, indicating that the  $(111)_{\gamma}$  planes are parallel to the  $(011)_{\delta}$  planes. This corresponds to the N-W OR, which has been previously reported in laser-engineered net shaping (LENS) fabricated 304L [61]. The bright-field TEM image shown in figure 3d reveals an elongated  $\delta$  particle located between two  $\gamma$  grains separated by a relatively planar interface. The SAED pattern in figure 3e at the circled region shows that the two  $\gamma$  grains are in a twin orientation relationship. The delta particle satisfies a K-S OR simultaneously with both  $\gamma$  grains, as evidenced by the alignment of the  $[11\bar{1}]_{\delta}$  axis and  $[011]_{\gamma}$  axis of both  $\gamma$  grains, and the superimposed (011)-type  $\delta$  and (111)-type  $\gamma$ diffraction spots. These results demonstrate the possible formation of  $\Sigma 3$  boundaries in the solid-state, via K-S V1/V2 selection. Unlike annealing twin boundaries, these K-S V1/V2 boundaries are topologically wavy and hence exhibit numerous {112} incoherent segments, highlighted in figure 3d. A third OR was also found in as-built 304L, presented using EBSD in figure 3f,g and using a step size of 70 nm. Figure 3f,g show corresponding IPF-colored and phase maps of a region where small remnant  $\delta$  particles are aligned along the cell boundaries of the  $\gamma$  grain. These particles are likely the primary  $\delta$  cell cores that nucleated and grew as dendrites in the liquid [62] at the onset of the FA-type solidification [48]. In this region,  $\gamma$  and  $\delta$  phases show nearly identical IPF colors and all three sets of their (100) directions are perfectly aligned, drawn in figure 3g, therefore revealing a cube-on-cube OR. Such OR implies that both  $\gamma$  and  $\delta$  phases in figure 3f,g nucleated directly from the liquid and grew following the temperature gradient.

Table 1: Enumeration of 24 possible K-S variants [56, 59], corresponding inter-variant axis-angle rotation, and inter-variant boundary length fraction measured experimentally.

Variants	FCC/BCC parallel planes	FCC/BCC parallel directions	Rotation angle/axis from V1	Note	316 variant boundary percentage	304 variant boundary percentage
V1	(1 1 1) <sub>FCC</sub> //(0 1 1) <sub>BCC</sub>	$[\bar{1}\ 0\ 1]_{FCC}//[\bar{1}\ \bar{1}\ 1]_{BCC}$	-	-	-	_
V2	$(1\ 1\ 1)_{FCC}//(0\ 1\ 1)_{BCC}$	$[\bar{1}\ 0\ 1]_{FCC}//[\bar{1}\ 1\ \bar{1}]_{BCC}$	60°/[1 1 1̄]	-	0.11	14.84
V3	$(1\ 1\ 1)_{FCC}//(0\ 1\ 1)_{BCC}$	$[0\ 1\ \bar{1}]_{FCC}//[\bar{1}\ \bar{1}\ 1]_{BCC}$	60°/[0 1 1]	V3 = V5	0.02	0.08
V4	$(1\ 1\ 1)_{FCC}//(0\ 1\ 1)_{BCC}$	$[0\ 1\ \overline{1}]_{FCC}//[\overline{1}\ 1\ \overline{1}]_{BCC}$	10.5°/[0 Ī Ī]	- /	0.15	0.32
V5	$(1\ 1\ 1)_{FCC}//(0\ 1\ 1)_{BCC}$	$[1\ \overline{1}\ 0]_{FCC}//[\overline{1}\ \overline{1}\ 1]_{BCC}$	60°/[0 Ī Ī]	V5 = V3	0.02	0.08
V6	$(1\ 1\ 1)_{FCC}//(0\ 1\ 1)_{BCC}$	$[1\ \overline{1}\ 0]_{FCC}//[\overline{1}\ 1\ \overline{1}]_{BCC}$	49.5°/[0 1 1]	-	0.14	0.06
V7	$(1\ \overline{1}\ 1)_{FCC}//(0\ 1\ 1)_{BCC}$	$[1\ 0\ \overline{1}]_{FCC}//[\overline{1}\ \overline{1}\ 1]_{BCC}$	49.5°/[Ī Ī 1]	-	0.02	0.09
V8	$(1\ \overline{1}\ 1)_{FCC}//(0\ 1\ 1)_{BCC}$	$[1\ 0\ \overline{1}]_{FCC}//[\overline{1}\ 1\ \overline{1}]_{BCC}$	10.5°/[1 1 1]		0.14	0.32
V9	$(1\ \bar{1}\ 1)_{FCC}//(0\ 1\ 1)_{BCC}$	$[\bar{1}\ \bar{1}\ 0]_{FCC}//[\bar{1}\ \bar{1}\ 1]_{BCC}$	50.5°/[10 3 13]	V9 = V19	0.19	0.13
V10	$(1\ \bar{1}\ 1)_{FCC}//(0\ 1\ 1)_{BCC}$	$[\bar{1}\ \bar{1}\ 0]_{FCC}//[\bar{1}\ 1\ \bar{1}]_{BCC}$	50.5°/[7̄ 5̄ 5]	V10 = V14	0.10	0.08
V11	$(1\ \bar{1}\ 1)_{FCC}//(0\ 1\ 1)_{BCC}$	$[0\ 1\ 1]_{FCC}//[\bar{1}\ \bar{1}\ 1]_{BCC}$	14.9°/[13 5 1]	V11 = V13	0.67	0.43
V12	$(1\ \bar{1}\ 1)_{FCC}//(0\ 1\ 1)_{BCC}$	$[0\ 1\ 1]_{FCC}//[\bar{1}\ 1\ \bar{1}]_{BCC}$	57.2°[3̄ 5 6]	V12 = V20	0.19	0.13
V13	$(\bar{1}\ 1\ 1)_{FCC}//(0\ 1\ 1)_{BCC}$	$[0\ \overline{1}\ 1]_{FCC}//[\overline{1}\ \overline{1}\ 1]_{BCC}$	14.9°/[5 13 Ī]	V13 = V11	0.67	0.43
V14	$(\bar{1}\ 1\ 1)_{FCC}//(0\ 1\ 1)_{BCC}$	$[0\ \overline{1}\ 1]_{FCC}//[\overline{1}\ 1\ \overline{1}]_{BCC}$	50.5°/[5̄ 5 7̄]	V14 = V10	0.1	0.08
V15	$(\bar{1}\ 1\ 1)_{FCC}//(0\ 1\ 1)_{BCC}$	$[\bar{1}\ 0\ \bar{1}]_{FCC}//[\bar{1}\ \bar{1}\ 1]_{BCC}$	57.2°/[6 2 5]	V15 = V23	0.16	0.2
V16	$(\bar{1}\ 1\ 1)_{FCC}//(0\ 1\ 1)_{BCC}$	$[\bar{1}\ 0\ \bar{1}]_{FCC}//[\bar{1}\ 1\ \bar{1}]_{BCC}$	20.6°/[11 11 6]	/ -	0.42	0.15
V17	$(\bar{1}\ 1\ 1)_{FCC}//(0\ 1\ 1)_{BCC}$	$[1\ 1\ 0]_{FCC}//[\bar{1}\ \bar{1}\ 1]_{BCC}$	51.7°/[IĪ1 6 IĪ1]	_	0.03	0.07
V18	$(\bar{1}\ 1\ 1)_{FCC}//(0\ 1\ 1)_{BCC}$	[1 1 0] <sub>FCC</sub> //[Ī 1 Ī] <sub>BCC</sub>	47.1°/[24 10 21]	V18 = V22	0.26	0.17
V19	$(1\ 1\ \overline{1})_{FCC}//(0\ 1\ 1)_{BCC}$	[Ī 1 0] <sub>FCC</sub> //[Ī Ī 1] <sub>BCC</sub>	50.5°/[3 13 10]	V19 = V9	0.19	0.13
V20	$(1\ 1\ \overline{1})_{FCC}//(0\ 1\ 1)_{BCC}$	$[\bar{1}\ 1\ 0]_{FCC}//[\bar{1}\ 1\ \bar{1}]_{BCC}$	57.2°/[3 6 5]	V20=V12	0.19	0.13
V21	$(1\ 1\ \overline{1})_{FCC}//(0\ 1\ 1)_{BCC}$	$[0\ \overline{1}\ \overline{1}]_{FCC}//[\overline{1}\ \overline{1}\ 1]_{BCC}$	20.6°/[3 0 1]	-	0.43	0.16
V22	$(1\ 1\ \overline{1})_{FCC}//(0\ 1\ 1)_{BCC}$	[0 Ī Ī] <sub>FCC</sub> //[Ī 1 Ī] <sub>BCC</sub>	47.1°/[10 21 24]	V22=V18	0.26	0.17
V23	$(1\ 1\ \overline{1})_{FCC}//(0\ 1\ 1)_{BCC}$	[1 0 1] <sub>FCC</sub> //[Ī Ī 1] <sub>BCC</sub>	57.2°/[2̄ 5̄ 6̄]	V23 = V15	0.16	0.2
V24	$(1\ 1\ \overline{1})_{FCC}//(0\ 1\ 1)_{BCC}$	[1 0 1] <sub>FCC</sub> //[Ī 1 Ī] <sub>BCC</sub>	21.1°/[9 4̄ 0]	-	0.2	0.18

Table 2: Enumeration of 12 possible N-W variants [60], corresponding inter-variant axis-angle rotation, and inter-variant boundary length fraction measured experimentally.

Variants	FCC BCC plane parallel	FCC BCC direction parallel	Rotation angle/axis from V1	Note	316 Variant boundary percentage	304 Variant boundary percentage
V1	(1 1 1) <sub>FCC</sub> //(0 1 1) <sub>BCC</sub>	[10 Ī] <sub>FCC</sub> //[100] <sub>BCC</sub>	=	=	=	=
V2	(1 1 1) <sub>FCC</sub> //(0 1 1) <sub>BCC</sub>	[1 1 0] <sub>FCC</sub> //[100] <sub>BCC</sub>	60°/[1 0 1]	V1 = V2	0.02	0.46
V3	(1 1 1) <sub>FCC</sub> //(0 1 1) <sub>BCC</sub>	[0 1 1] <sub>FCC</sub> //[100] <sub>BCC</sub>	$60^{\circ}/[\bar{1}\ 0\ 1]$	V1 = V2	0.02	0.46
V4	(1 1 1) <sub>FCC</sub> //(0 1 1) <sub>BCC</sub>	[1 0 1] <sub>FCC</sub> //[100] <sub>BCC</sub>	13.76°/[12 1 12]	V4 = V10	0.23	1.58
V5	(1 1 1) <sub>FCC</sub> //(0 1 1) <sub>BCC</sub>	[1 1 0] <sub>FCC</sub> //[100] <sub>BCC</sub>	50.05°/[4 3 4]	V5 = V12	0.08	0.40
V6	(1 1 1) <sub>FCC</sub> //(0 1 1) <sub>BCC</sub>	[0 1 Ī] <sub>FCC</sub> //[100] <sub>BCC</sub>	53.69°/[Ī 3 3]	V6 = V8 = V9 = V11	0.10	0.39
V7	(1 Ī 1) <sub>FCC</sub> //(0 1 1) <sub>BCC</sub>	[Ī 0 1] <sub>FCC</sub> //[100] <sub>BCC</sub>	19.47°/[0 0 1]	-	0.41	0.95
V8	(1 Ī 1) <sub>FCC</sub> //(0 1 1) <sub>BCC</sub>	[1 1 0] <sub>FCC</sub> //[100] <sub>BCC</sub>	53.69°/[3 1 3]	V6 = V8 = V9 = V11	0.10	0.39
V9	$(1\bar{1}1)_{FCC}//(011)_{BCC}$	[0 Ī Ī] <sub>FCC</sub> //[100] <sub>BCC</sub>	53.69°/[3 1 3]	V6 = V8 = V9 = V11	0.10	0.39
V10	$(1\ 1\ \bar{1})_{FCC}//(0\ 1\ 1)_{BCC}$	[Ī 0 Ī] <sub>FCC</sub> //[100] <sub>BCC</sub>	13.76°/[12 1 12]	V10 = V4	0.23	1.58
V11	(1 1 Ī) <sub>FCC</sub> //(0 1 1) <sub>BCC</sub>	[1 Ī 0] <sub>FCC</sub> //[100] <sub>BCC</sub>	53.69°/[1 3 3]	V6 = V8 = V9 = V11	0.10	0.39
V12	$(1\ 1\ \bar{1})_{FCC}//(0\ 1\ 1)_{BCC}$	[0 1 1] <sub>FCC</sub> //[100] <sub>BCC</sub>	50.05°/[4 3 4]	V12 = V5	0.08	0.40

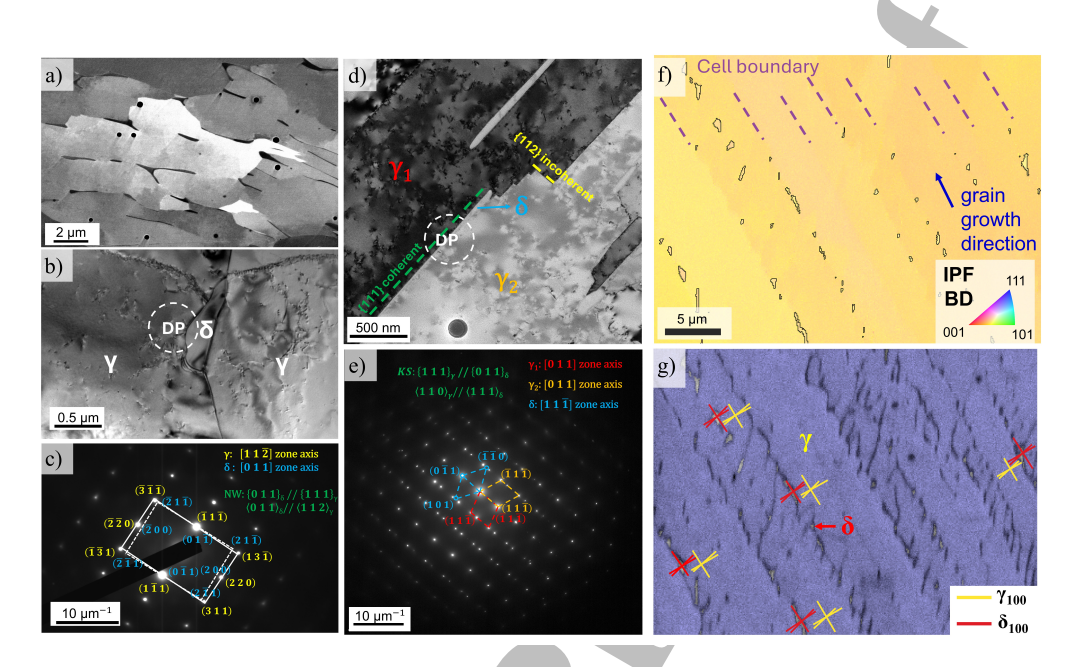


Figure 3:  $\delta - \gamma$  orientation relationships (ORs) found in AM 304L. a) Back-scattered SEM image, showing  $\delta$  ferrite at cellular boundaries and grain boundaries, b) bright-field TEM image of a ferrite particle located between two austenite grains, c) SAED diffraction pattern taken around the circled area in a ferrite particle located between two twin-related austenite grains, d) bright-field TEM image of a ferrite needle located on the boundary between two austenite grains, e) SAED pattern showing a ferrite particle simultaneously satisfying K-S OR with both twin-related austenite grains, f) EBSD IPF and g) corresponding phase map of a large grain in AM 304L. Phase boundaries and cell boundaries are highlighted with black and purple lines in f), and the  $\langle 100 \rangle$  crystal directions are highlighted in both phases in g).

Considering that some  $\gamma$  grains nucleated directly from the liquid, the next two sections investigate the possibility of whether this direct liquid to  $\gamma$  transition could contribute to the formation of  $\Sigma 3$  boundaries.

#### 3.4. Structure of twin-related grain clusters

A closer inspection of the as-built 304L microstructure reveals that  $\Sigma 3$  boundaries bind together large twin-related grain clusters. Two examples of such clusters are shown in figure 4 and figure 5. In the first cluster, shown in IPF colors in figure 4a,  $\Sigma 3$  boundaries and HAGBs are highlighted using white and black lines, respectively. This cluster is composed of five grains, numbered in the figure, that developed close to the bottom of the melt pool (highlighted with a grey dashed line). While grains 1-4 appear as continuous regions throughout the observation plane, grain 5 possesses a more serrated shape, which can be attributed to a cross-sectioning artifact. Hence we identify regions 5' and 5", that possess the same crystallographic orientation as 5 and likely belong to the same grain in 3D.  $\Sigma 3$  boundaries exhibit a curved and tortuous morphology, which differs substantially from the classic morphology of annealing and deformation twins. This is consistent with the intense grain boundary serration previously reported in DED-printed 304L [44].

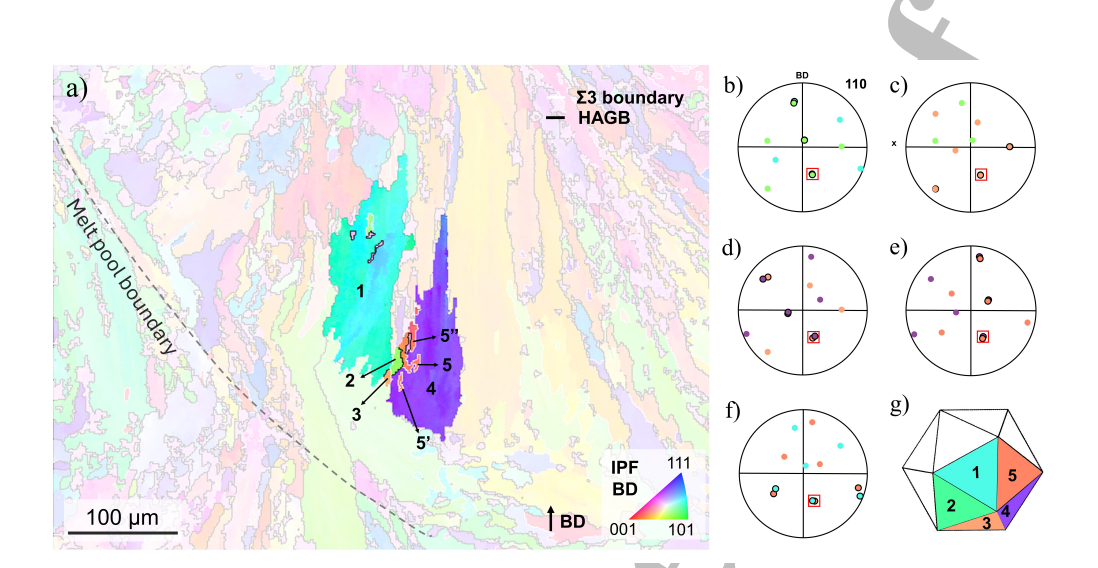


Figure 4: Representative example of a twin-related grain cluster in AM 304L. a) EBSD IPF map of a cluster of twin-related grains, highlighted via transparency. b-f) Pairwise (110) pole figures of grains b) 1 & 2, c) 2 & 3, d) 3 & 4, e) 4 & 5, f) 5 & 1. Poles highlighted with dark solid lines indicate common (111) twin planes, showing a near-twin relationship. The common (110) direction is indicated with a red box on all pole figures. g) Icosahedron nucleation motif with five faces colored based on the IPF color of grains 1-5.

To better understand the orientation relationships within the grain cluster, pair-wise (110) pole figures (PFs) are plotted in figure 4b-f, using the average orientation of each grain. Figure 4b) corresponds to grains 1 & 2, c) to grains 2& 3, etc. The contours of the three (110) poles, which define the shared (111) planes (twin planes) for each pair of grains, are highlighted in black on the PFs. This reveals a twin OR between grain 1 & 2, 2 & 3, 3 & 4, and 4 & 5. Grains 1 & 5 have a near-twin relationship due to incomplete overlap of the three highlighted (110) directions, as shown in figure 4f. Remarkably, these five grains share a common (110) direction, which is highlighted with a red box in all PFs. This reveals a five-fold orientation symmetry around this common (110) direction within the cluster. A second cluster of twin-related grains with slightly more complex geometry is presented in figure 5. Again, this cluster is composed of five individual grains bounded two-by-two by  $\Sigma 3$  boundaries, which are highlighted with white lines in figure 5a. This cluster is located further away from the melt pool boundary and exhibits subsequent lattice rotation, indicated by the gradient in IPF color in grains 2 and 4, in particular. Such kind of lattice rotation is typical in DED 304L, as shown by Polonsky et al. [42], and more prominent in grains that are affected by remelting during the AM process. Grains 4 and 4', despite showing slightly different IPF colors, are believed to be part of a single grain, due to significant overlap in their (110) pole figures (PF) in figure 5e and f. Grains 3 and 3' are characterized by a globular morphology and appear as inclusions within grains 2 and 4. They exhibit the same crystallographic orientation. Figure 5b-f reveals a common {111} plane between grains 1 & 2, 2 & 3, 3' & 4, 4' & 5, as well as 5 & 1 despite being located 300 µm apart. Similarly to the previous cluster, these grains also exhibit a characteristic 5-fold

orientation symmetry around a common  $\langle 110 \rangle$  direction, highlighted with a red box in figure 5b-f. Since K-S V1/V2 is the only inter-variant boundary that could contribute to  $\Sigma 3$ , this mechanism can only create one pair of twin-related grains. Thus, it cannot explain the 5-fold orientation symmetry observed within these twin clusters.

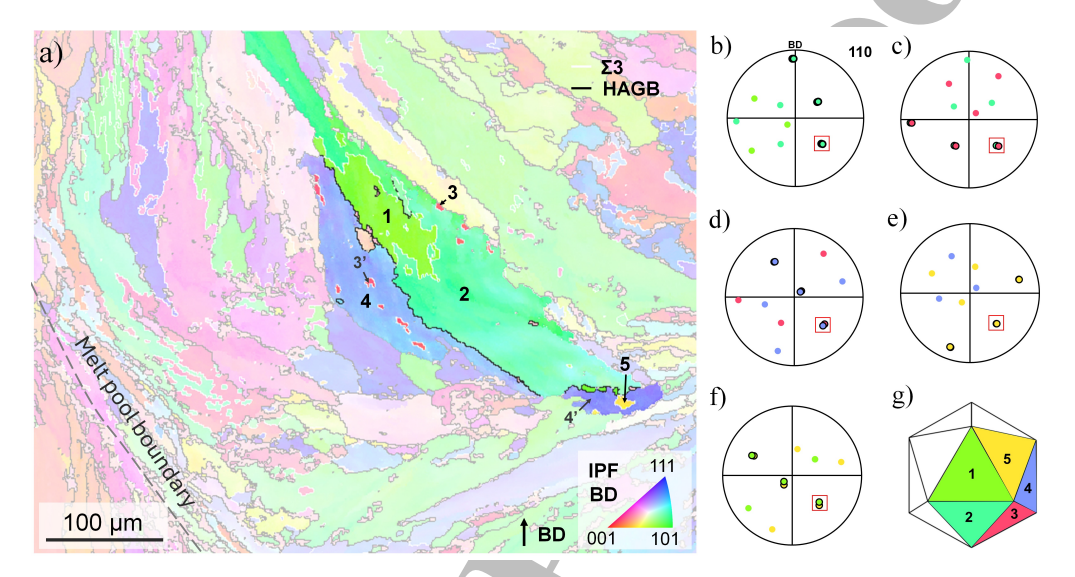


Figure 5: Twin-related grain cluster in AM 304L. a) EBSD IPF map showing the cluster via transparency. b-f) Pairwise  $\langle 110 \rangle$  pole figures of grains b) 1 & 2, c) 2 & 3, d) 3' & 4, e) 4' & 5, and f) 5 & 1. Poles highlighted with dark solid lines indicate common  $\langle 111 \rangle$  planes. The common  $\langle 110 \rangle$  direction is framed in a red box. g) Icosahedron with five faces colored based on the IPF color of grains 1-5.

#### 4. Discussion

#### 4.1. Nucleation mechanism of twin-related grain clusters

Groups of twin-related grains manifesting a five-fold orientation symmetry around a common  $\langle 110 \rangle$  direction is a characteristic configuration known to arise from a peculiar nucleation mechanism in undercooled molten metals, called icosahedral short-range order (ISRO)-mediated nucleation. In this mechanism, identified by Rappaz et al. [63], short-range ordering in the undercooled melt is a necessary condition [63–68]. The solidification of metallic materials was traditionally believed to originate from a fully disordered liquid. In 1952, Frank [69] hypothesized that ISRO in the liquid would explain the large undercoolings measured by Turnbull and Fisher [70] in metallic melts. ISRO was then experimentally revealed using in-situ high-energy X-ray diffraction as well as neutron scattering [71–73] during levitation melting. In 2013, Kurtuldu et al. [64] demonstrated for the first time that the structure of the solidifying liquid directly affects the final microstructure. They showed that minor additions of Cr (0.1 wt.%) in a Al-20wt.% Zn lead to ISRO in the undercooled liquid, serving as a precursor to the formation of icosahedral quasicrystals (iQCs), or their approximant stable phase  $Al_{45}Cr_7$  [63, 64, 74], a complex intermetallic. Upon further cooling, heteroepitaxial

growth of FCC grains on the iQC template results in a drastically refined microstructure, an abnormally high fraction of  $\Sigma 3$  boundaries, and multiple twin-related grains with 5-fold orientation symmetry around a common  $\langle 011 \rangle$  axis [63, 64, 74]. Kurtuldu et al. then reported a similar microstructure when adding minute additions of Ir in an Au-Cu-Ag alloy. In this system, no iQCs or approximant stable phases have been reported to date [63, 74]. This indicates that FCC grains may form through heteroepitaxial growth on an icosahedral template, directly resulting from ISRO in an undercooled liquid. Deeper undercooling in the liquid generally increases the degree of ISRO and thus promotes ISRO-mediated nucleation [63, 72]. Initially proposed by Kurtuldu et al. [63, 64, 74], this mechanism is illustrated in figure 6.

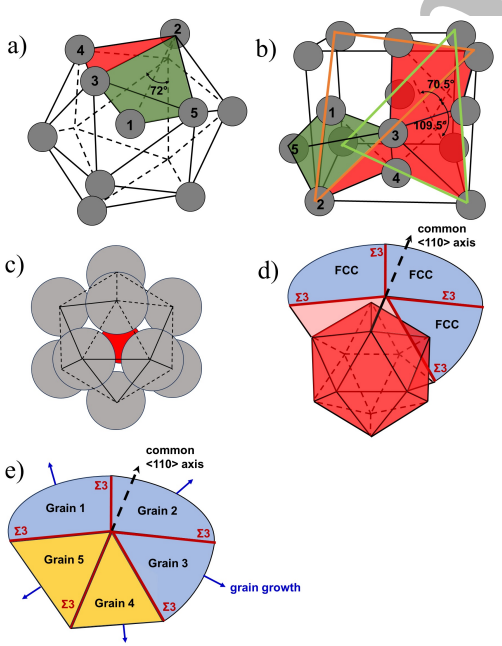


Figure 6: Schematic representation of ISRO-mediated nucleation, adapted from Rappaz et al. [63]. The gray spheres represent the atoms in both the a) icosahedral and b) FCC unit cells; c) short-range ordering in the liquid forming an icosahedral motif, d) nucleation of FCC grains on each triangular facet of the icosahedron template with a heteroepitaxy relationship, resulting in pairs of twin-related grains, e) icosahedral template disappearing during solidification, leaving a cluster of twin-related grains with five-fold symmetry around a common axis of the original icosahedron.

Atoms in the liquid first agglomerate to form icosahedral motifs shown in figure 6a, which may form a solid-state icosahedral quasicrystal or remain in the liquid state [63] depending on the alloy's chemistry. As solidification proceeds in the undercooled liquid, FCC crystals (shown in figure 6b) nucleate on the triangular facets of the icosahedral motif following a heteroepitaxy relationship, as sketched in figure 6c,d. The epitaxial growth of FCC grains occurs such that their {111} planes and  $\langle 110 \rangle$  edges grow parallel to the icosahedron's triangular facets and edges. Due to

the unique geometric relationship between the icosahedral motif and the FCC unit cell, as we will discuss in detail in the following paragraphs, adjacent FCC grains share a common (110) axis inherited from their icosahedral nucleation template, and are paired in a close-to twin relationship. Considering that FCC crystals can nucleate and grow on any of the 20 equilateral triangular facets of the icosahedral motif, ISRO-mediated nucleation is a powerful mechanism that can simultaneously explain the origin of grain refinement and a large fraction of  $\Sigma 3$  boundaries during solidification of undercooled liquids [63]. Depending on the thermodynamics and the nature of the icosahedral template (actual solid quasicrystal or local ordering of atoms in the liquid), the icosahedral template disappears during solidification, leaving only a characteristic signature in the form of twin-related grains with five-fold orientation symmetry around a common (110) direction[63]. The geometric relationship between the icosahedron and FCC unit cell plays a critical role in the nucleation process. As figure 6a shows, a regular icosahedron contains 20 equilateral triangular facets, with axes connecting opposite vertices forming five-fold symmetry axes. Tetrahedra are formed by a central atom and its three nearest vertices, linked by faces with its nearest neighbor (e.g., red and green tetrahedra, bounded by atoms 1-2-3-4 and 1-2-3-5). They possess a mutual angle of 72° between their internal faces (e.g., 1-2-3 and 1-2-5) in order to complete a 360° rotation with a five-fold symmetry [63]. These tetrahedra are slightly distorted compared with the FCC tetrahedral structures shown in figure 6b. The latter are bounded by the {111} planes, linked to their neighbors via (110) axes, and have their {111} planes either 70.5° or 109.5° apart. Densely packed {111} planes in an FCC structure adopts an ABCABC... stacking sequence. A and B layers are denoted with green and orange triangles in figure 6b. Atoms in the front left corner and back right corner are in the C layer. When a new green tetrahedron is attached to the structure with a coinciding {111} plane, analogous to the two colored tetrahedrons in figure 6b, a stacking fault is induced, which changes the stacking sequence to ABCABACB, thereofore leading to the formation of twins on the shared {111} plane [63]. Proving the occurrence of ISRO-mediated nucleation requires the identification of a cluster of neighboring grains that are twin-related and share a five-fold orientation symmetry around a common (110) direction [64, 65, 67, 75]. Such evidence is shown in both figure 4 and figure 5. The icosahedral template for each grain cluster is shown in figure 4g and figure 5g, where each facet is colored based on the grains average IPF color. It should be noted that besides the possibility of a sectioning artifact, the drastic contrast in grain sizes in figure 5a may arise from the ISRO-induced stacking fault mechanism. This mechanism implies that ISRO motifs in the liquid can attach directly to the growing FCC crystals, creating a stacking fault that leads to the formation of  $\Sigma$ 3 boundaries between a large grain that has already grown, and small grains that just nucleated [63, 75, 76]. This would explain the inclusion-like grains 3 and 3' in figure 5. ISRO-mediated nucleation can also explain the near-twin orientation relationship between 

grains 5 and 1 in figure 5a -numbered first and last grains intentionally. According to figure 5f, the two {111} planes

have rotated slightly with respect to the common (110) direction. This near-twin orientation relationship between the

first and last grains in ISRO-induced clusters has been previously reported and can be explained by the accumulated

angular difference between the 5 tetrahedra of the icosahedron ( $72 \times 5 = 360^{\circ}$ ) and the 5 {111} tetrahedra in the

complex approximant phase, this would imply that the icosahedral nucleation template is induced by local ordering in the solidifying liquid. To conclude, compelling evidence confirms the occurrence of ISRO-mediated nucleation in the as-built 304L microstructure. This mechanism is known to contribute significantly to both grain refinement and the formation of  $\Sigma$ 3 boundaries, both found in FA-type microstructures. In the next section, we discuss the relationship between the solidification mode and ISRO in the solidifying liquid.

#### 4.2. Linkage between ISRO and the FA solidification mode

Figure 1b shows a substantial surge in  $\Sigma 3$  boundary fraction when switching from an AF to a FA solidification mode. To explain this trend, we plot in figure 7a,b, the weight fraction of the two major alloy elements in austenitic stainless steels -Cr and Ni- against the molar fraction of liquid for a FA and an AF-type solidification under Scheil's assumptions. A dashed line separates the phase regions. At the onset of FA solidification, the primary  $\delta$  solidification front absorbs Cr but rejects Ni into the liquid [48], as shown in figure 7a, leading to a local reduction in the Cr/Ni ratio in the liquid ahead of the solidification front. On the other hand, the partition coefficients of Cr and Ni are smaller than unity for the  $\gamma$  phase, indicating that both elements are rejected in the liquid during the growth of the  $\gamma$  phase [48, 51, 77, 78]. This leads to the increase of Cr and Ni when  $\gamma$  grain start to nucleate and grow in the liquid, as observed in figure 7b and in the  $L + \delta + \gamma$  region in figure 7a. This indicates that the solidification mode locally alters the composition of the liquid ahead of the solidification front in FeCrNi alloys.

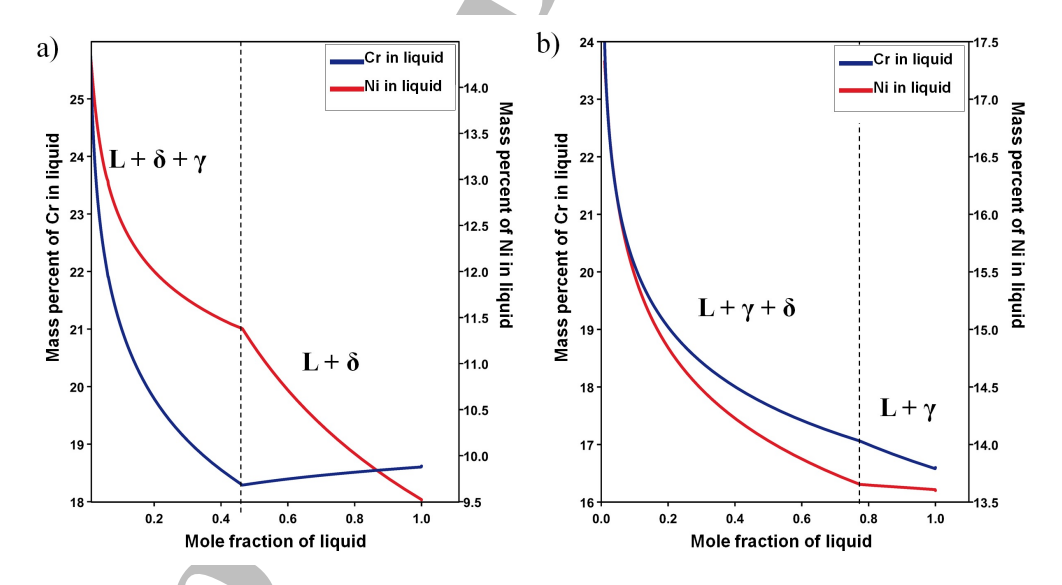


Figure 7: Thermocalc calculations of Scheil solidification of a) FA and b) AF solidification modes. The dashed line separates the two-phase and three-phase coexistence regions during the solidification process. The local concentration of Cr and Ni are plotted in blue and red, respectively.

Jeon et al. [79] studied the structure of the liquid in undercooled electrostatically levitated  $Fe_{72}Cr_xNi_{1-x}$  melts

using in-situ high-energy synchrotron X-ray diffraction. By analyzing the excess volume and the structure factor, they concluded that FeCrNi melts generally show ISRO, and a lower Cr content in the liquid (i.e. a lower Cr/Ni ratio) corresponds to a higher degree of local ordering [79]. This is in agreement with our experimental observations: ISRO-mediated nucleation is only found in microstructures solidied in FA mode. In this mode, Cr partitions towards the primary  $\delta$  ferrite at the onset of solidification, resulting in a continuous reduction of the Cr/Ni ratio in the liquid as the volume fraction of  $\delta$  ferrite increases. This behavior is captured in the L +  $\delta$  region in figure 7a. According to Jeong et al., this local decrease in Cr is prone to triggering a higher degree of ISRO in the liquid [79], thus promoting ISRO-mediated nucleation during the subsequent solidification of the  $\gamma$  phase [63, 74]. It should be mentioned that the Scheil calculation assumes no diffusion in solids and infinite diffusion in liquids, which is not strictly true and should be treated as a theoretical limit. Reduced segregation (particularly under high solidification rates) and diffusion are to be expected in solids [80], realistically. However, this model reasonably captures the effect of solute partitioning during solidification and the effect of the solidification mode. In conclusion, the FA-type solidification mode plays a critical role in the formation of  $\Sigma 3$  boundaries directly from the liquid. This is achieved by forming a transient primary  $\delta$  phase, which increases the degree of ISRO in the liquid by consuming Cr, facilitating ISRO-mediated nucleation locally. The combination of this mechanism in the liquid-state with the impingement of K-S V1/V2  $\gamma$ variants via a solid-phase transformation, leads to the sharp increase in  $\Sigma 3$  boundary length fraction in figure 2, precisely corresponding to the shift from the AF to the FA solidification mode. Recognizing that both solid-state and liquid-state mechanisms contribute to the formation of \$\Sigma\$3 boundaries, we delve into the morphology of the twin domains in the section below. 4.3. On the origin of globular twin domains and wavy boundaries

While relying on 2D EBSD characterization poses significant challenges in identifying the origin of each  $\Sigma 3$  boundary, examining the morphology of the twin domains and their neighboring grains may provide valuable insights into the metallurgical mechanisms responsible for their formation. All grains and  $\Sigma 3$  boundaries observed in FA-type microstructures are serrated (i.e., tortuous), which is a remarkable feature. This implies that all grains, including twin-related grains, possess a characteristic globular morphology, as highlighted in figures 1b, 3, 4, and 5. Grains 3 and 3' in figure 5a are characteristic examples. These two grains are simultaneously twinned with grains 2 and 4. Such a configuration cannot be explained by the K-S V1/V2 solid-state mechanism, which can only account for one single pair of twin-related grains. Instead, this configuration is a clear evidence of ISRO-mediated nucleation. Conversely, the IPF-colored map in figure 8 reveals the other globular twin morphology commonly found in as-printed FA-type microstructures, solely composed of two distinct orientations (purple and yellow). Neither of these two grain orientations shows any twin relationship with other neighboring grains. Thus, these two grains are likely the product of the solid-state mechanism, and originate from a single  $\delta$  ferrite orientation. Nevertheless, drawing conclusions based on 2D EBSD data is not always accurate due to the lack of information about the 3D grain structure and complete connectivity between grain neighbors. Observing twin-related grains exhibiting a full five-fold symmetry

provides compelling evidence of ISRO-mediated nucleation. However, the presence of only a pair of twin-related grains does not constitute proof of the absence of ISRO. Indeed, it is currently not known whether ISRO-mediated nucleation invariably results in the formation of five grains, particularly in AM conditions where not all five grains may be exposed to a favorable temperature gradient for their growth. We aim to investigate these aspects further through 3D EBSD characterization.

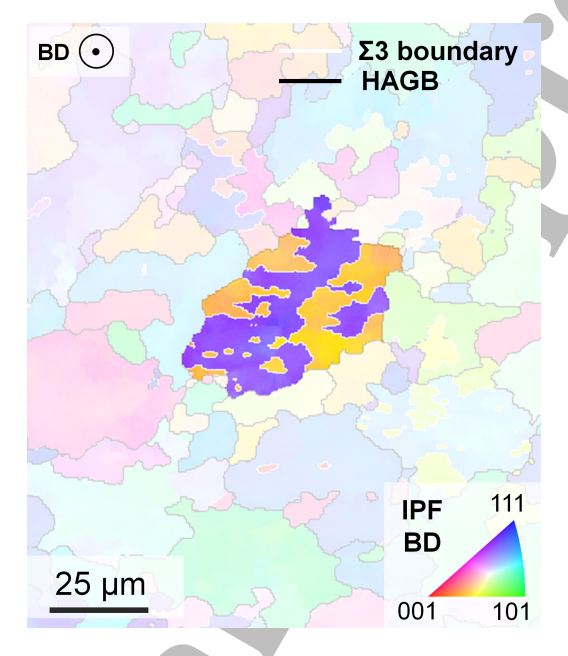


Figure 8: EBSD IPF map showing a globular twin domain in 304L, HAGB and  $\Sigma 3$  boundaries are shown in black and white lines, respectively.

Recognizing that two different mechanisms may produce globular twin domains, we explore the origin of the wavy  $\Sigma 3$  boundaries. Remarkably, all observed  $\Sigma 3$  boundaries exhibit a wavy appearance, similar to other HAGBs depicted in figures 4, 5, and 8. This contrasts with findings from previous literature where  $\Sigma 3$  boundaries are formed in the liquid-state (ISRO) or solid-state (K-S V1/V2). For example, Cazic et al. [67, 68] found ISRO-induced  $\Sigma 3$  boundaries with a planar morphology in DED AM Inconel 718. Kurtuldu et al. [74] also present ISRO-induced  $\Sigma 3$  boundaries with a rather planar morphology in cast Au-Cu-Ag alloys [74]. On the other hand, Haghdadi et al. observed K-S V1/V2-induced  $\Sigma 3$  boundaries in a duplex stainless steel, also clearly planar [56]. Here, we attribute the serrated morphology of  $\Sigma 3$  boundaries to remnant  $\delta$  ferrite particles hindering the growth of austenite grains via a Smith-Zener pinning mechanism, as reported in our previous study [44]. The tortuous twin boundary morphology indicates that the as-built FA-solidified alloys contain a relatively high density of incoherent segments compared with conventional GBE microstructures [3], clearly visible in figure 3d. This could result in unique GBE-related properties, such as resistance to fatigue crack growth or hydrogen embrittlement, which is the scope of our current research.

### 4.4. Microstructure and phase evolution during solidification

The extent of undercooling in the metallic melt is closely related to the degree of ISRO in the liquid [72], and it plays a central role in ISRO-mediated nucleation [63, 69, 74]. Patel et al. developed a methodology to capture the effect of undercooling in the melt pool of laser spot welding during rapid solidification [81]. They observed that the extent of undercooling is the highest closest to the melt pool boundary at the beginning of solidification. As solidification progresses, the melt pool shrinks relative to its center, leading to lower undercooling due to the release of latent heat resulting from nucleation and solidification [81]. Under this assumption, we would expect to observe ISROinduced grain clusters in the most undercooled regions of the melt pool, i.e. at its boundaries [81]. EBSD data acquired at the melt pool scale in 304L is presented in figure 9, where the melt pool boundary highlighted with dashed lines. The twin-related grain clusters appear to originate primarily from regions that are close to the melt pool boundary, similar to what is also shown in figure 4 and 5. In addition to a reduced degree of undercooling, the competitive growth of grains can also contribute to the lower fraction of  $\Sigma 3$  boundaries towards the center of the melt, depending on the local directionality of the temperature gradient [82-84]. As a result, the initial ISRO-induced grain clusters can be replaced by non-twinned grains as solidification proceeds. Furthermore, the accumulation of intragranular misorientation during grain growth [42] can also disrupt the original twin relationship. Interestingly, despite the widely reported effect of ISRO-mediated nucleation on microstructure refinement [63, 64, 66-68, 74], figure 9 reveals that the twinned dendrites located closer to the melt pool boundary do not exhibit a refined microstructure when compared with grains located towards the center of the melt pool. This discrepancy arises from variations in grain size and growth mode due to different temperature gradients (G) and grain growth rates (R) across the melt pool. In laser-processed microstructures, a transition from large columnar to fine equiaxed grains occurs from the melt pool boundary to the centerline due to a continuous decrease in the G/R ratio [85, 86]. To summarize, the microstructure formation of FA-type microstructures can be pictured as follows: i) primary  $\delta$  phase nucleates and grows with one of its (100) direction following the steepest temperature gradient at the onset of FA-type solidification, locally absorbing Cr and rejecting Ni into the liquid; ii) the local depletion in Cr promotes ISRO in the liquid, locally; iii) ISRO-mediated nucleation triggers the formation of twinned y grains clusters, refining the microstructure; iv) a solid-state primary  $\delta$ into  $\gamma$  transformation occurs with preferred ORs, where the encounter of K-S V1/V2 variants creates additional  $\Sigma 3$ boundaries. The exact fraction of  $\Sigma$ 3 boundaries formed by either mechanism requires 3D analyzes, which is the focus of future studies.

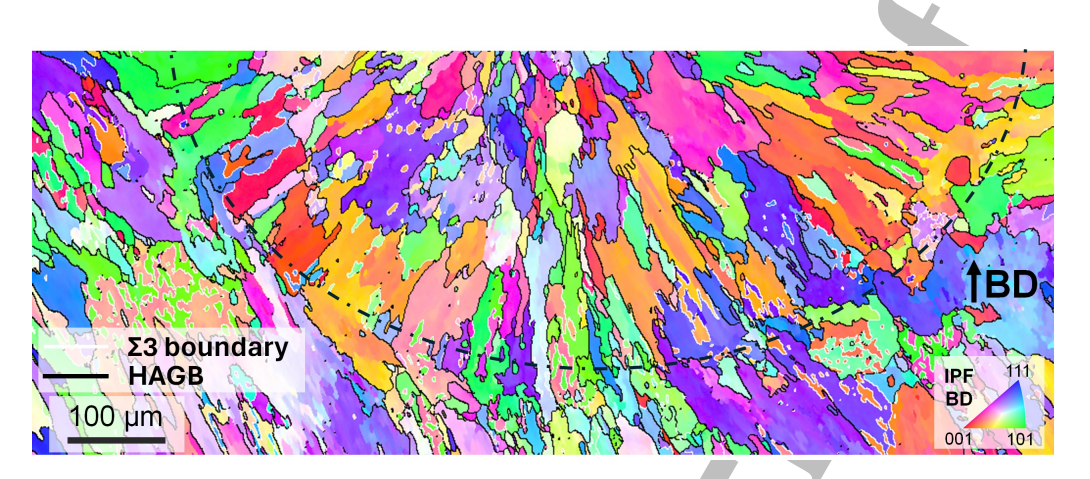
 

Figure 9: EBSD IPF map showing a melt pool in as-printed 304L. Σ3 boundaries and HAGBs are highlighted using white and black lines, respectively; and the melt pool boundary is highlighted with a black dashed line.

#### 5. Conclusion

We reveal that the FA-type solidification mode governs the microstructure development in AM FeNiCr stainless steels, resulting in finer grain structures characterized by a high density of  $\Sigma 3$  boundaries. We identify two metallurgical mechanisms at the origin of this phenomenon, one operating in the solid-state, the other in the liquid-state. First, a strong variant selection following a Kurdjimov-Sachs orientation relationship in the ferrite-to-austenite phase transformation leads to the formation of twin boundaries upon the encounter of twin-related austenite variants formed from a common parent ferrite orientation. This process takes place during the AM process as the initial ferrite becomes unstable and transforms to austenite upon cooling. Second, we provide direct evidence of austenite grains solidifying directly from the liquid. Prior ferrite formation in the solidification sequence locally depletes the solidifying liquid from Cr, which increases icosahedral short-range ordering as austenite grain nucleate. Local liquid ordering is at the origin of austenite twin clusters, composed of groups of grains exhibiting a characteristic five-fold orientation symmetry around a common (011) axis, inherited from the isocahedral seed template. Beyond shedding light on the metallurgical mechanisms at the origin of grain refinement and  $\Sigma 3$  boundary formation in AM FeNiCr alloys, these findings allow to identify new alloy design strategies for AM as well as new pathways to tailor the mechanical properties and resistance to environmental attack of AM alloys via grain boundary engineering.

#### 6. Acknowledgements

We gratefully acknowledge support from the National Science Foundation, CAREER award DMR-2236640. We acknowledge the use of facilities and instrumentation at the Materials Research Laboratory Central Research Facilities at the University of Illinois.

1			
2 3 4	405	Ref	erences
5	406	[1]	T. Watanabe, Grain boundary engineering: historical perspective and future prospects, Journal of Materials Science 46 (12) (2011) 4095–4115.
6 7	407		doi:10.1007/s10853-011-5393-z.
8	408		URL http://dx.doi.org/10.1007/s10853-011-5393-z
9	409	[2]	C. A. Schuh, M. Kumar, W. E. King, Analysis of grain boundary networks and their evolution during grain boundary engineering, Acta
10 11	410		Materialia 51 (3) (2003) 687-700. doi:10.1016/s1359-6454(02)00447-0.
12	411		URL http://dx.doi.org/10.1016/S1359-6454(02)00447-0
13	412	[3]	$N.\ Bozzolo, M.\ Bernacki, Viewpoint on the formation and evolution of annealing twins during thermomechanical processing of fcc metals and the formation of $
14 15	413		alloys, Metallurgical and Materials Transactions A: Physical Metallurgy and Materials Science 51 (2020) 2665–2684. doi:10.1007/s11661-
16	414		020-05772-7.
17	415	[4]	M. Laleh, A. E. Hughes, M. Y. Tan, G. S. Rohrer, S. Primig, N. Haghdadi, Grain boundary character distribution in an additively manufactured
18	416		austenitic stainless steel, Scripta Materialia 192 (2021) 115–119. doi:10.1016/j.scriptamat.2020.10.018.
19 20	417		URL http://dx.doi.org/10.1016/j.scriptamat.2020.10.018
21	418	[5]	S. Gao, Z. Hu, M. Duchamp, P. S. R. Krishnan, S. Tekumalla, X. Song, M. Seita, Recrystallization-based grain boundary engineering of 316l
22	419		stainless steel produced via selective laser melting, Acta Materialia 200 (2020) 366–377. doi:10.1016/j.actamat.2020.09.015.
23	420		URL http://dx.doi.org/10.1016/j.actamat.2020.09.015
24 25	421	[6]	M. Qian, J. Lippold, The effect of annealing twin-generated special grain boundaries on haz liquation cracking of nickel-base superalloys,
26	422		Acta Materialia 51 (12) (2003) 3351–3361. doi:10.1016/s1359-6454(03)00090-9.
27	423		URL http://dx.doi.org/10.1016/S1359-6454(03)00090-9
28	424	[7]	V. Thaveeprungsriporn, G. S. Was, The role of coincidence-site-lattice boundaries in creep of ni-16cr-9fe at 360 °c, Metallurgical and Mate-
29 30	425		rials Transactions A 28 (10) (1997) 2101–2112. doi:10.1007/s11661-997-0167-6.
31	426		URL http://dx.doi.org/10.1007/s11661-997-0167-6
32	427	[8]	S. Spigarelli, M. Cabibbo, E. Evangelista, G. Palumbo, Analysis of the creep strength of a low-carbon aisi 304 steel with low- $\sigma$ grain
33	428		boundaries, Materials Science and Engineering: A 352 (1–2) (2003) 93–99. doi:10.1016/s0921-5093(02)00903-6.
34 35	429		URL http://dx.doi.org/10.1016/S0921-5093(02)00903-6
36	430	[9]	M. Seita, J. P. Hanson, S. Gradečak, M. J. Demkowicz, The dual role of coherent twin boundaries in hydrogen embrittlement, Nature
37	431		Communications 6 (1). doi:10.1038/ncomms7164.
38 39	432		URL http://dx.doi.org/10.1038/ncomms7164
40	433	[10]	V. Randle, Twinning-related grain boundary engineering, Acta Materialia 52 (14) (2004) 4067–4081. doi:10.1016/j.actamat.2004.05.031.
41	434		URL http://dx.doi.org/10.1016/j.actamat.2004.05.031
42	435	[11]	R. Jones, V. Randle, Sensitisation behaviour of grain boundary engineered austenitic stainless steel, Materials Science and Engineering: A
43 44	436		527 (16–17) (2010) 4275–4280. doi:10.1016/j.msea.2010.03.058.
45	437		URL http://dx.doi.org/10.1016/j.msea.2010.03.058
46	438	[12]	X. Chen, J. Li, X. Cheng, B. He, H. Wang, Z. Huang, Microstructure and mechanical properties of the austenitic stainless steel 316l fabricated
47	439		by gas metal arc additive manufacturing, Materials Science and Engineering: A 703 (2017) 567–577. doi:10.1016/j.msea.2017.05.024.
48 49	440		URL http://dx.doi.org/10.1016/j.msea.2017.05.024
50	441	[13]	Y. M. Wang, T. Voisin, J. T. McKeown, J. Ye, N. P. Calta, Z. Li, Z. Zeng, Y. Zhang, W. Chen, T. T. Roehling, R. T. Ott, M. K. Santala,
51	442		P. Depond, M. J. Matthews, A. V. Hamza, T. Zhu, Additively manufactured hierarchical stainless steels with high strength and ductility,
52	443		Nature Materials 17 (1) (2017) 63–71. doi:10.1038/nmat5021.
53 54	444		URL http://dx.doi.org/10.1038/nmat5021
55	445	[14]	Z. Li, B. He, Q. Guo, Strengthening and hardening mechanisms of additively manufactured stainless steels: The role of cell sizes, Scripta
56	446		Materialia 177 (2020) 17–21. doi:10.1016/j.scriptamat.2019.10.005.
57	447		URL http://dx.doi.org/10.1016/j.scriptamat.2019.10.005
58 59			20

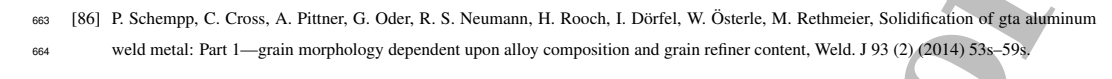
1 2			
3	440	[15]	K. Bertsch, G. Meric de Bellefon, B. Kuehl, D. Thoma, Origin of dislocation structures in an additively manufactured austenitic stainless
4	448	[13]	steel 316l, Acta Materialia 199 (2020) 19–33. doi:10.1016/j.actamat.2020.07.063.
5	449		
6 7	450	[16]	URL http://dx.doi.org/10.1016/j.actamat.2020.07.063
8	451	[10]	D. Kong, C. Dong, S. Wei, X. Ni, L. Zhang, R. Li, L. Wang, C. Man, X. Li, About metastable cellular structure in additively manufactured
9	452		austenitic stainless steels, Additive Manufacturing 38 (2021) 101804. doi:10.1016/j.addma.2020.101804.
10	453	£1.73	URL http://dx.doi.org/10.1016/j.addma.2020.101804
11 12	454	[1/]	X. Zou, Z. Yan, K. Zou, W. Liu, L. Song, S. Li, L. Cha, Grain refinement by dynamic recrystallization during laser direct energy deposition
13	455		of 316l stainless steel under thermal cycles, Journal of Manufacturing Processes 76 (2022) 646–655. doi:10.1016/j.jmapro.2022.01.057.
14	456		URL http://dx.doi.org/10.1016/j.jmapro.2022.01.057
15	457	[18]	Y. L. Hu, X. Lin, X. F. Lu, S. Y. Zhang, H. O. Yang, L. Wei, W. D. Huang, Evolution of solidification microstructure and dynamic recrys-
16	458		tallisation of inconel 625 during laser solid forming process, Journal of Materials Science 53 (22) (2018) 15650–15666. doi:10.1007/s10853-
17 18	459		018-2701-x.
19	460		URL http://dx.doi.org/10.1007/s10853-018-2701-x
20	461	[19]	N. Kouraytem, J. Varga, B. Amin-Ahmadi, H. Mirmohammad, R. A. Chanut, A. D. Spear, O. T. Kingstedt, A recrystallization
21	462		heat-treatment to reduce deformation anisotropy of additively manufactured inconel 718, Materials & Design 198 (2021) 109228
22 23	463		doi:10.1016/j.matdes.2020.109228.
24	464		URL http://dx.doi.org/10.1016/j.matdes.2020.109228
25	465	[20]	D. D. Peachey, C. P. Carter, A. Garcia-Jimenez, A. Mukundan, D. N. Leonard, MA. Charpagne, Z. C. Cordero, Directional recrystallization
26	466		of an additively manufactured ni-base superalloy, Additive Manufacturing 60 (2022) 103198. doi:10.1016/j.addma.2022.103198.
27	467		URL http://dx.doi.org/10.1016/j.addma.2022.103198
28 29	468	[21]	O. Messé, R. Muñoz-Moreno, T. Illston, S. Baker, H. Stone, Metastable carbides and their impact on recrystallisation in in738lc processed
30	469		by selective laser melting, Additive Manufacturing 22 (2018) 394-404. doi:10.1016/j.addma.2018.05.030.
31	470		URL http://dx.doi.org/10.1016/j.addma.2018.05.030
32	471	[22]	L. S. Aota, P. Bajaj, K. D. Zilnyk, E. A. Jägle, D. Ponge, H. R. Z. Sandim, D. Raabe, Recrystallization kinetics, mechanisms
33 34	472		and topology in alloys processed by laser powder-bed fusion: Aisi 316l stainless steel as example, Materialia 20 (2021) 101236
35	473		doi:10.1016/j.mtla.2021.101236.
36	474		URL http://dx.doi.org/10.1016/j.mtla.2021.101236
37	475	[23]	MA. Charpagne, JM. Franchet, N. Bozzolo, Overgrown grains appearing during sub-solvus heat treatment in a polycrystalline $\gamma - \gamma'$
38 39	476		nickel-based superalloy, Materials & Design 144 (2018) 353–360. doi:10.1016/j.matdes.2018.02.048.
40	477		URL http://dx.doi.org/10.1016/j.matdes.2018.02.048
41	478	[24]	H. E. Sabzi, N. T. Aboulkhair, X. Liang, XH. Li, M. Simonelli, H. Fu, P. E. Rivera-Díaz-del Castillo, Grain refinement in laser powder bed
42	479		fusion: The influence of dynamic recrystallization and recovery, Materials & Design 196 (2020) 109181. doi:10.1016/j.matdes.2020.109181
43	480		URL http://dx.doi.org/10.1016/j.matdes.2020.109181
44 45	481	[25]	W. H. Kan, D. Jiang, M. Humbert, X. Gao, V. K. Bhatia, G. Proust, Y. Zhu, P. Hodgson, A. Huang, Effect of in-situ layer-by-layer rolling or
46	482		the microstructure, mechanical properties, and corrosion resistance of a directed energy deposited 316l stainless steel, Additive Manufacturing
47	483		55 (2022) 102863. doi:10.1016/j.addma.2022.102863.
48	484		URL http://dx.doi.org/10.1016/j.addma.2022.102863
49 50	485	[26]	C. Li, Y. Tian, Y. Chen, P. Hodgson, X. Wu, Y. Zhu, A. Huang, Hierarchical layered and refined grain structure of inconel 718 superalloy
51	486		produced by rolling-assisted directed energy deposition, Additive Manufacturing Letters 1 (2021) 100009. doi:10.1016/j.addlet.2021.100009
52	487		URL http://dx.doi.org/10.1016/j.addlet.2021.100009
53	488	[27]	L. S. Aota, P. Bajaj, K. D. Zilnyk, D. Ponge, H. R. Z. Sandim, The origin of abnormal grain growth upon thermomechanical processing of
54 55	489		laser powder-bed fusion alloys, Materialia 20 (2021) 101243. doi:10.1016/j.mtla.2021.101243.
56	490		URL http://dx.doi.org/10.1016/j.mtla.2021.101243
57			
58			21
59 60			21
60 61			
62			
63			
64			
65			

1 2			
3	491	[28]	S. Gao, Z. Li, S. Van Petegem, J. Ge, S. Goel, J. V. Vas, V. Luzin, Z. Hu, H. L. Seet, D. F. Sanchez, H. Van Swygenhoven, H. Gao, M. Seita,
4 5	492		Additive manufacturing of alloys with programmable microstructure and properties, Nature Communications 14 (1). doi:10.1038/s41467-
6	493		023-42326-у.
7	494		URL http://dx.doi.org/10.1038/s41467-023-42326-y
8	495	[29]	D. Brandon, The structure of high-angle grain boundaries, Acta Metallurgica 14 (11) (1966) 1479–1484. doi:https://doi.org/10.1016/0001-
9	496		6160(66)90168-4.
10 11	497		URL https://www.sciencedirect.com/science/article/pii/0001616066901684
12	498	[30]	Z. Li, T. Voisin, J. T. McKeown, J. Ye, T. Braun, C. Kamath, W. E. King, Y. M. Wang, Tensile properties, strain rate sensitiv-
13	499		ity, and activation volume of additively manufactured 316l stainless steels, International Journal of Plasticity 120 (2019) 395-410.
14 15	500		doi:10.1016/j.ijplas.2019.05.009.
16	501		URL http://dx.doi.org/10.1016/j.ijplas.2019.05.009
17	502	[31]	J. K. Mackenzie, Second paper on statistics associated with the random disorientation of cubes, Biometrika 45 (1/2) (1958) 229.
18	503		doi:10.2307/2333059.
19 20	504		URL http://dx.doi.org/10.2307/2333059
21	505	[32]	Z. Yan, K. Zou, M. Cheng, Z. Zhou, L. Song, Revealing relationships between heterogeneous microstructure and strengthening mechanism of
22	506		austenitic stainless steels fabricated by directed energy deposition (ded), Journal of Materials Research and Technology 15 (2021) 582-594.
23	507		doi:10.1016/j.jmrt.2021.08.036.
24 25	508	[33]	V. Randle, Mechanism of twinning-induced grain boundary engineering in low stacking-fault energy materials, Acta Materialia 47 (15–16)
26	509		(1999) 4187–4196. doi:10.1016/s1359-6454(99)00277-3.
27	510		URL http://dx.doi.org/10.1016/S1359-6454(99)00277-3
28	511	[34]	D. Molnár, X. Sun, S. Lu, W. Li, G. Engberg, L. Vitos, Effect of temperature on the stacking fault energy and deformation behaviour in 3161
29 30	512		austenitic stainless steel, Materials Science and Engineering: A 759 (2019) 490–497. doi:10.1016/j.msea.2019.05.079.
31	513		URL http://dx.doi.org/10.1016/j.msea.2019.05.079
32	514	[35]	M. Kumar, A. J. Schwartz, W. E. King, Microstructural evolution during grain boundary engineering of low to medium stacking fault energy
33	515		fcc materials, Acta Materialia 50 (10) (2002) 2599–2612. doi:10.1016/s1359-6454(02)00090-3.
34 35	516		URL http://dx.doi.org/10.1016/S1359-6454(02)00090-3
36	517	[36]	J. Jung, J. I. Yoon, J. G. Kim, M. I. Latypov, J. Y. Kim, H. S. Kim, Continuum understanding of twin formation near grain boundaries of fcc
37	518		metals with low stacking fault energy, npj Computational Materials 3 (1). doi:10.1038/s41524-017-0023-1.
38 39	519		URL http://dx.doi.org/10.1038/s41524-017-0023-1
40	520	[37]	M. Charpagne, A. Polonsky, M. Echlin, S. Jacomet, J. d. Jaeger, M. De Graef, N. Bozzolo, T. Pollock, Growth accidents induced by primary
41	521		$\gamma^{\prime\prime}$ precipitates in a polycrystalline nickel-based superalloy, Scripta Materialia 186 (2020) 109–113. doi:10.1016/j.scriptamat.2020.05.020.
42	522		URL http://dx.doi.org/10.1016/j.scriptamat.2020.05.020
43 44	523	[38]	Y. Jin, B. Lin, M. Bernacki, G. Rohrer, A. Rollett, N. Bozzolo, Annealing twin development during recrystallization and grain growth in pure
45	524		nickel, Materials Science and Engineering: A 597 (2014) 295-303. doi:10.1016/j.msea.2014.01.018.
46	525		URL http://dx.doi.org/10.1016/j.msea.2014.01.018
47	526	[39]	C. S. Pande, M. A. Imam, B. B. Rath, Study of annealing twins in fcc metals and alloys, Metallurgical Transactions A 21 (11) (1990)
48 49	527		2891–2896. doi:10.1007/bf02647209.
50	528		URL http://dx.doi.org/10.1007/BF02647209
51	529	[40]	DG. Ahn, Directed energy deposition (ded) process: State of the art, International Journal of Precision Engineering and Manufacturing-
52	530		Green Technology 8 (2) (2021) 703-742. doi:10.1007/s40684-020-00302-7.
53 54	531		URL http://dx.doi.org/10.1007/s40684-020-00302-7
55	532	[41]	S. Gaudez, K. A. Abdesselam, H. Gharbi, Z. Hegedüs, U. Lienert, W. Pantleon, M. V. Upadhyay, High-resolution reciprocal space mapping
56	533		reveals dislocation structure evolution during 3d printing, Additive Manufacturing 71 (2023) 103602. doi:10.1016/j.addma.2023.103602.
57 58			
59			22
60			
61			
62 63			
64			
65			

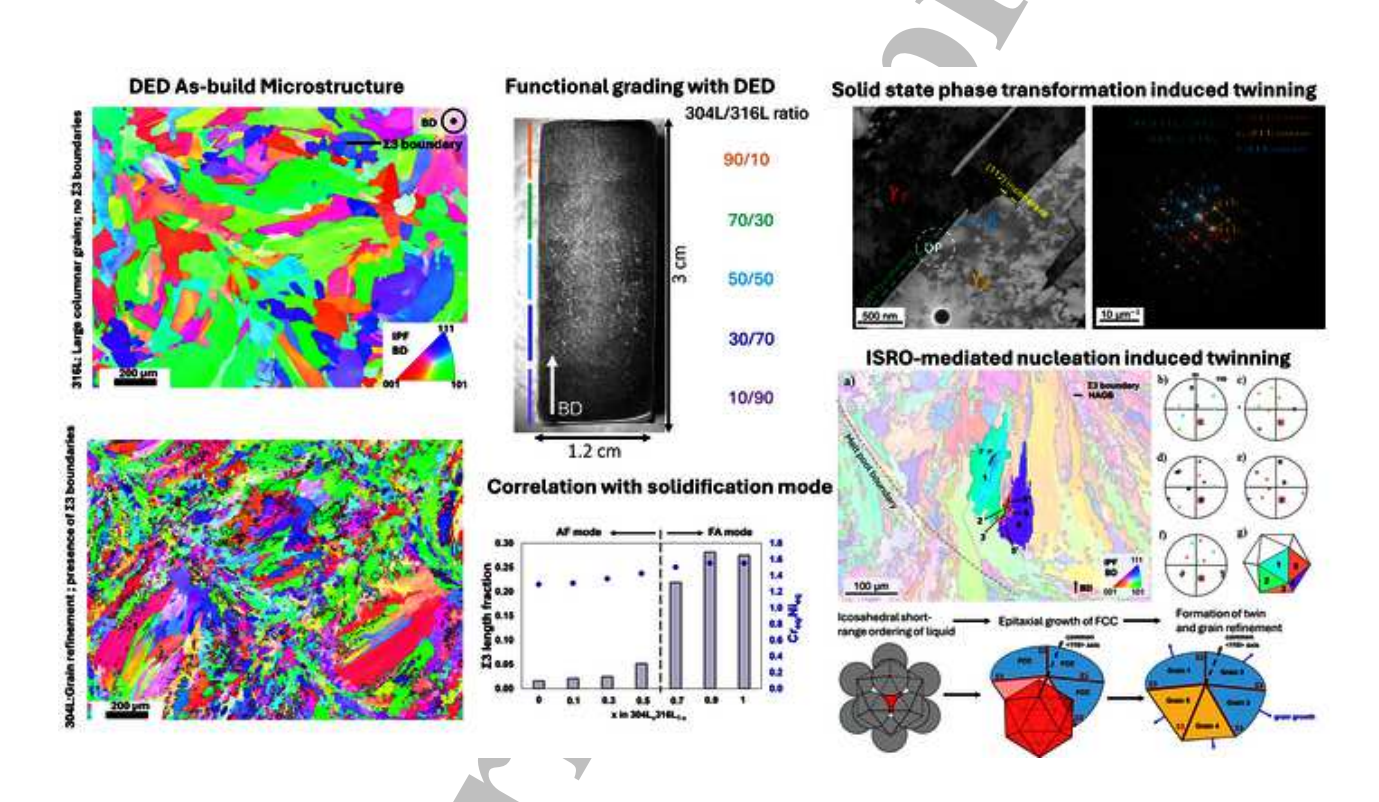
1			
2 3			
4	534		URL http://dx.doi.org/10.1016/j.addma.2023.103602
5	535	[42]	A. T. Polonsky, W. C. Lenthe, M. P. Echlin, V. Livescu, G. T. Gray, T. M. Pollock, Solidification-driven orientation gradients in additively
6	536		manufactured stainless steel, Acta Materialia 183 (2020) 249–260. doi:10.1016/j.actamat.2019.10.047.
7 8	537		URL http://dx.doi.org/10.1016/j.actamat.2019.10.047
9	538	[43]	S. Martin, A. Weidner, C. Ullrich, C. Schimpf, M. Motylenko, R. Lehnert, H. Biermann, D. Rafaja, A. Vinogradov, Y. Estrin, Deformation
10	539		behaviour of twip steels: Constitutive modelling informed by local and integral experimental methods used in concert, Materials Characteri-
11	540		zation 184 (2022) 111667. doi:10.1016/j.matchar.2021.111667.
12 13	541		URL http://dx.doi.org/10.1016/j.matchar.2021.111667
14	542	[44]	Y. Nie, Y. T. Chang, M. A. Charpagne, Functionally graded stainless steels with tailored grain boundary serration, Scripta Materialia 237.
15	543		doi:10.1016/j.scriptamat.2023.115714.
16	544	[45]	C. Lee, Y. Lee, C. Lee, S. Hong, Precipitation behavior of the sigma phase with ni and mn content variations in superaustenitic stainless steel
17 18	545		weld metal, Materials Characterization 144 (2018) 148–154. doi:10.1016/j.matchar.2018.07.006.
19	546		URL http://dx.doi.org/10.1016/j.matchar.2018.07.006
20	547	[46]	G. Jacob, Prediction of solidification phases in Cr-Ni stainless steel alloys manufactured by laser based powder bed fusion process, US
21	548		Department of Commerce, National Institute of Standards and Technology, 2018. doi:10.6028/nist.ams.100-14.
22 23	549		URL http://dx.doi.org/10.6028/NIST.AMS.100-14
24	550	[47]	Y. H. Kim, D. G. Kim, J. H. Sung, I. S. Kim, D. E. Ko, N. H. Kang, H. U. Hong, J. H. Park, H. W. Lee, Influences of cr/ni equivalent ratios of
25	551		filler wires on pitting corrosion and ductility-dip cracking of aisi 316l weld metals, Metals and Materials International 17 (1) (2011) 151–155.
26	552		doi:10.1007/s12540-011-0221-1.
27 28	553		URL http://dx.doi.org/10.1007/s12540-011-0221-1
29	554	[48]	J. A. Brooks, A. W. Thompson, Microstructural development and solidification cracking susceptibility of austenitic stainless steel welds,
30	555		International Materials Reviews 36 (1991) 16–44. doi:10.1179/imr.1991.36.1.16.
31	556	[49]	M. A. Melia, HD. A. Nguyen, J. M. Rodelas, E. J. Schindelholz, Corrosion properties of 304l stainless steel made by directed energy
32 33	557		deposition additive manufacturing, Corrosion Science 152 (2019) 20–30. doi:10.1016/j.corsci.2019.02.029.
34	558		URL http://dx.doi.org/10.1016/j.corsci.2019.02.029
35	559	[50]	M. Ghayoor, K. Lee, Y. He, Ch. Chang, B. K. Paul, S. Pasebani, Selective laser melting of 304l stainless steel: Role of volumetric energy den-
36	560		sity on the microstructure, texture and mechanical properties, Additive Manufacturing 32 (2020) 101011. doi:10.1016/j.addma.2019.101011.
37 38	561		URL http://dx.doi.org/10.1016/j.addma.2019.101011
39	562	[51]	T. R. Smith, J. D. Sugar, C. S. Marchi, J. M. Schoenung, Microstructural development in DED stainless steels: applying welding models
40	563		to elucidate the impact of processing and alloy composition, Journal of Materials Science 56 (1) (2020) 762–780. doi:10.1007/s10853-020-
41	564		05232-y.
42 43	565		URL https://doi.org/10.1007/s10853-020-05232-y
44	566	[52]	J. Yang, L. Hawkins, L. He, S. Mahmood, M. Song, K. Schulze, X. Lou, Intragranular irradiation-assisted stress corrosion cracking (iascc)
45	567		of 316l stainless steel made by laser direct energy deposition additive manufacturing: Delta ferrite-dislocation channel interaction, Journal of
46	568		Nuclear Materials 577 (2023) 154305. doi:10.1016/j.jnucmat.2023.154305.
47 48	569		URL http://dx.doi.org/10.1016/j.jnucmat.2023.154305
49	570	[53]	H. K. D. H. Bhadeshia, LE. Svensson, Mathematical Modelling of Weld Phenomena, CRC Press, 1993.
50	571		URL www.msm.cam.ac.uk/phase-trans.
51	572	[54]	H. Flower, T. Lindley, Electron backscattering diffraction study of acicular ferrite, bainite, and martensite steel microstructures, Materials
52 53	573		Science and Technology 16 (1) (2000) 26–40. doi:10.1179/026708300773002636.
54	574		URL http://dx.doi.org/10.1179/026708300773002636
55	575	[55]	N. Haghdadi, P. Cizek, P. D. Hodgson, Y. He, B. Sun, J. J. Jonas, G. S. Rohrer, H. Beladi, New insights into the interface characteristics
56 57	576		of a duplex stainless steel subjected to accelerated ferrite-to-austenite transformation, Journal of Materials Science 55 (2020) 5322-5339.
58			
59			23
60			
61 62			
63			
64			
65			

1 2			
3	577		doi:10.1007/s10853-020-04358-3.
4		[56]	N. Haghdadi, P. Cizek, P. D. Hodgson, V. Tari, G. S. Rohrer, H. Beladi, Five-parameter crystallographic characteristics of the in
5	578	[30]	
6 7	579		terfaces formed during ferrite to austenite transformation in a duplex stainless steel, Philosophical Magazine 98 (2018) 1284–1306
8	580		doi:10.1080/14786435.2018.1434321.
9	581	[57]	J. Y. Huang, Y. D. Yu, Y. K. Wu, H. Q. Ye, Z. F. Dong, Thermal decomposition of mechanically alloyed nanocrystalline fcc fe60cu40, Journal
10	582		of Materials Research 11 (11) (1996) 2717–2724. doi:10.1557/jmr.1996.0344.
11	583		URL http://dx.doi.org/10.1557/JMR.1996.0344
12 13	584	[58]	K. Koumatos, A. Muehlemann, A theoretical investigation of orientation relationships and transformation strains in steels, Acta Crystallo
14	585		graphica Section A Foundations and Advances 73 (2) (2017) 115–123. doi:10.1107/s2053273316020350.
15	586		URL http://dx.doi.org/10.1107/S2053273316020350
16	587	[59]	H. Beladi, G. S. Rohrer, A. D. Rollett, V. Tari, P. D. Hodgson, The distribution of intervariant crystallographic planes in a lath martensit
17	588		using five macroscopic parameters, Acta Materialia 63 (2014) 86-98. doi:10.1016/j.actamat.2013.10.010.
18 19	589	[60]	K. Koumatos, A. Muehlemann, A theoretical investigation of orientation relationships and transformation strains in steels, Acta Crystallo
20	590		graphica Section A Foundations and Advances 73 (2) (2017) 115–123. doi:10.1107/s2053273316020350.
21	591		URL http://dx.doi.org/10.1107/S2053273316020350
22	592	[61]	T. J. Headley, J. A. Brooks, A new bcc-fcc orientation relationship observed between ferrite and austenite in solidification structures of steels
23	593		Metallurgical and Materials Transactions A 33 (1) (2002) 5–15. doi:10.1007/s11661-002-0001-0.
24 25	594		URL http://dx.doi.org/10.1007/s11661-002-0001-0
26	595	[62]	H. Kokawa, T. Kuwana, A. Yamamoto, Crystallographic characteristics of delta-ferrite transformations in a 304l weld metal at elevate
27	596		temperatures, Weld. J 68 (3).
28	597	[63]	M. Rappaz, P. Jarry, G. Kurtuldu, J. Zollinger, Solidification of metallic alloys: Does the structure of the liquid matter?, Metallurgical and
29	598		Materials Transactions A 51 (6) (2020) 2651–2664. doi:10.1007/s11661-020-05770-9.
30 31	599		URL http://dx.doi.org/10.1007/s11661-020-05770-9
32	600	[64]	G. Kurtuldu, P. Jarry, M. Rappaz, Influence of cr on the nucleation of primary al and formation of twinned dendrites in al–zn–cr alloys: Ca
33	601	[]	icosahedral solid clusters play a role?, Acta Materialia 61 (19) (2013) 7098–7108. doi:10.1016/j.actamat.2013.07.056.
34	602		URL http://dx.doi.org/10.1016/j.actamat.2013.07.056
35 36	603	[65]	C. Galera-Rueda, X. Jin, J. LLorca, M. Pérez-Prado, Icosahedral quasicrystal enhanced nucleation in commercially pure ni processed by
37		[03]	selective laser melting, Scripta Materialia 211 (2022) 114512. doi:10.1016/j.scriptamat.2022.114512.
38	604		
39	605	[66]	URL http://dx.doi.org/10.1016/j.scriptamat.2022.114512
40	606	[66]	M. Buttard, G. Martin, X. Bataillon, G. Renou, P. Lhuissier, J. Villanova, B. Chehab, P. Jarry, JJ. Blandin, P. Donnadieu, Towards an allo
41 42	607		design strategy by tuning liquid local ordering: What solidification of an al-alloy designed for laser powder bed fusion teaches us, Additiv
43	608		Manufacturing 61 (2023) 103313. doi:10.1016/j.addma.2022.103313.
44	609		URL http://dx.doi.org/10.1016/j.addma.2022.103313
45	610	[67]	I. Cazic, J. Zollinger, S. Mathieu, M. El Kandaoui, P. Plapper, B. Appolaire, New insights into the origin of fine equiaxed microstructures in
46	611		additively manufactured inconel 718, Scripta Materialia 195 (2021) 113740. doi:10.1016/j.scriptamat.2021.113740.
47 48	612		URL http://dx.doi.org/10.1016/j.scriptamat.2021.113740
49	613	[68]	I. Cazic, J. Zollinger, M. Engstler, J. Ghanbaja, T. Schenk, M. El Kandaoui, B. Appolaire, Nucleation burst in additively man
50	614		ufactured inconel 718: 3d characterization of isro-induced equiaxed microstructure, Additive Manufacturing 66 (2023) 103458
51	615		doi:10.1016/j.addma.2023.103458.
52	616		URL http://dx.doi.org/10.1016/j.addma.2023.103458
53 54	617	[69]	F. C. Frank, Supercooling of liquids, Proceedings of the Royal Society of London. Series A. Mathematical and Physical Sciences 215 (1120)
55	618		(1952) 43–46.
56	619	[70]	D. Turnbull, J. C. Fisher, Rate of nucleation in condensed systems, The Journal of chemical physics 17 (1) (1949) 71–73.
57			

1 2			
3	620	[71]	S. Krishnan, D. L. Price, X-ray diffraction from levitated liquids, Journal of Physics: Condensed Matter 12 (12) (2000) R145-R176
4	621		doi:10.1088/0953-8984/12/12/201.
5 6	622		URL http://dx.doi.org/10.1088/0953-8984/12/12/201
7	623	[72]	T. Schenk, D. Holland-Moritz, V. Simonet, R. Bellissent, D. M. Herlach, Icosahedral short-range order in deeply undercooled metallic melts
8	624		Physical Review Letters 89 (7). doi:10.1103/physrevlett.89.075507.
9	625		URL http://dx.doi.org/10.1103/PhysRevLett.89.075507
10 11	626	[73]	G. W. Lee, A. K. Gangopadhyay, K. F. Kelton, R. W. Hyers, T. J. Rathz, J. R. Rogers, D. Robinson, Difference in icosahedral short-range
12	627		order in early and late transition metal liquids, Physical Review Letters 93 (3). doi:10.1103/physrevlett.93.037802.
13	628		URL http://dx.doi.org/10.1103/PhysRevLett.93.037802
14	629	[74]	G. Kurtuldu, A. Sicco, M. Rappaz, Icosahedral quasicrystal-enhanced nucleation of the fcc phase in liquid gold alloys, Acta Materialia 70
15 16	630		(2014) 240–248. doi:10.1016/j.actamat.2014.02.037.
17	631		URL http://dx.doi.org/10.1016/j.actamat.2014.02.037
18	632	[75]	L. Monier, M. Buttard, M. Veron, J. J. Blandin, G. Martin, F. Villaret, Y. Shen, B. Yrieix, C. Ernould, J. Guyon, A. Despres, On the origin of
19	633	[]	grain refinement and twin boundaries in as-fabricated austenitic stainless steels produced by laser powder bed fusion, Additive Manufacturing
20 21	634		61. doi:10.1016/j.addma.2022.103351.
22	635	[76]	F. Royer, J. Zollinger, B. Rouat, M. Rappaz, Influence of minor cr additions on crystal growth in rapidly solidified al-20zn alloys, Materials
23	636	[,0]	13 (2) (2020) 379. doi:10.3390/ma13020379.
24	637		URL http://dx.doi.org/10.3390/ma13020379
25 26	638	[77]	Y. Arata, F. Matsuda, S. Katayama, Solidification crack susceptibility in weld metals of fully austenitic stainless steels, (1), Trans. JWRI (Jpn
27	639	[,,]	Weld. Res. Inst.) 5 (2) (1976) 135–151.
28	640	[78]	P. L. Ferrandini, C. T. Rios, A. T. Dutra, M. A. Jaime, P. R. Mei, R. Caram, Solute segregation and microstructure of directionally solidified
29		[70]	austenitic stainless steel, Materials Science and Engineering A 435-436 (2006) 139–144. doi:10.1016/j.msea.2006.07.024.
30	641	[70]	
31 32	642	[/9]	S. Jeon, M. P. Sansoucie, O. Shuleshova, I. Kaban, D. M. Matson, Density, excess volume, and structure of fe-cr-ni melts, The Journal of Chamical Division 152 (0). doi:10.1063/1.5140787
33	643		Chemical Physics 152 (9). doi:10.1063/1.5140787.
34	644	1001	URL http://dx.doi.org/10.1063/1.5140787
35	645	[8U]	T. Keller, G. Lindwall, S. Ghosh, L. Ma, B. M. Lane, F. Zhang, U. R. Kattner, E. A. Lass, J. C. Heigel, Y. Idell, M. E. Williams, A. J
36 37	646		Allen, J. E. Guyer, L. E. Levine, Application of finite element, phase-field, and calphad-based methods to additive manufacturing of ni-based
38	647		superalloys, Acta Materialia 139 (2017) 244–253. doi:10.1016/j.actamat.2017.05.003.
39	648	5013	URL http://dx.doi.org/10.1016/j.actamat.2017.05.003
40	649	[81]	S. Patel, P. Reddy, A. Kumar, A methodology to integrate melt pool convection with rapid solidification and undercooling kinetics in laser
41	650		spot welding, International Journal of Heat and Mass Transfer 164 (2021) 120575. doi:10.1016/j.ijheatmasstransfer.2020.120575.
42 43	651		URL http://dx.doi.org/10.1016/j.ijheatmasstransfer.2020.120575
44	652		T. DebRoy, S. David, Physical processes in fusion welding, Reviews of modern physics 67 (1) (1995) 85.
45	653	[83]	H. Wei, J. Elmer, T. DebRoy, Origin of grain orientation during solidification of an aluminum alloy, Acta Materialia 115 (2016) 123–131
46	654		doi:10.1016/j.actamat.2016.05.057.
47 48	655		URL http://dx.doi.org/10.1016/j.actamat.2016.05.057
49	656	[84]	P. Liu, Y. Ji, Z. Wang, C. Qiu, A. Antonysamy, LQ. Chen, X. Cui, L. Chen, Investigation on evolution mechanisms of site
50	657		specific grain structures during metal additive manufacturing, Journal of Materials Processing Technology 257 (2018) 191-202
51	658		doi:10.1016/j.jmatprotec.2018.02.042.
52 53	659		URL http://dx.doi.org/10.1016/j.jmatprotec.2018.02.042
54	660	[85]	Y. He, M. Zhong, N. Jones, J. Beuth, B. Webler, The columnar-to-equiaxed transition in melt pools during laser powder bed fusion of m2
55	661		steel, Metallurgical and Materials Transactions A 52 (9) (2021) 4206–4221. doi:10.1007/s11661-021-06380-9.
56	662		URL http://dx.doi.org/10.1007/s11661-021-06380-9
57			



**Graphical Abstract** 



Declaration of interests
oxtimes The authors declare that they have no known competing financial interests or personal relationships that could have appeared to influence the work reported in this paper.
☐ The author is an Editorial Board Member/Editor-in-Chief/Associate Editor/Guest Editor for [Journal name] and was not involved in the editorial review or the decision to publish this article.
☐ The authors declare the following financial interests/personal relationships which may be considered as potential competing interests: